

## ABSTRACT

SUBRAMANYAN, HARISH. Understanding Macro-to-Nano Scale Thermal Transport. (Under the direction of Dr. Jun Liu).

Over the past few decades, industries have strived to scaled down the size of their devices and increase their computational capabilities. This miniaturization is accompanied by large quantities of heat dissipation which can affect the lifetime and reliability of the devices. This compels a knowledge of thermal management for different length-scales.

Thermal design of a medium-frequency transformer is first studied to reinforce concepts of heat transfer at the macro-scale. The importance of thermal models is depicted through the application of Space Mapping. Analytical and FEA models are combined to yield a new design point with higher accuracy and reduced computational time.

Interface resistance gains significance as devices shrink down to the micro-scale. An improved model for calculating interfacial thermal conductance between interfaces formed by metals and low-dimensional materials is proposed. This anisotropic model uses full dispersion relations of the materials involved to conduct a mode-to-mode comparison and calculate the transmission probabilities. The model predicted thermal conductance values significantly closer to experimental measurements.

Thermal properties differ significantly at the nanoscale compared to their bulk counterparts. We utilize this phenomenon to improve upon the low thermal conductivity of polymers, by artificially restricting the angular bending freedom. An increase in chain stiffness and restriction of segmental rotations was responsible for improvement of thermal conductivity. A phonon transport analysis was then conducted to study the effect of increasing the angular bending potential on the group velocity and phonon dispersion curves. It was observed that angular bending potential was critical for regulating thermal transport in polymers.

© Copyright 2019 by Harish Subramanyan

All rights reserved

Understanding Macro-to-Nano Scale Thermal Transport

by  
Harish Subramanyan

A thesis submitted to the Graduate Faculty of  
North Carolina State University  
in partial fulfillment of the  
requirements for the degree of  
Master of Science

Mechanical Engineering

Raleigh, North Carolina

2019

APPROVED BY:

---

Dr. Jun Liu  
Chair of Advisory Committee

---

Dr. Brendan O'Connor

---

Dr. Xiaoning Jiang

## **DEDICATION**

*To my family*

## **BIOGRAPHY**

Harish Subramanyan was born in the city of Chennai located in southern India, in the year 1995 and grew up in Kolkata. His passion for Mechanical Engineering initiated at a very young age where his desire to know the working of everything he came across encouraged him to choose the Science stream in High School. He later earned his Bachelor's degree in Mechanical Engineering from SRM University, Chennai. His interest in heat transfer and the importance of thermal management motivated him to pursue a Master's degree at North Carolina State University. His research in a nutshell involves investigating the different methods involved in studying thermal transport at different length scales. Apart from research, Harish likes travelling, reading fiction novels, and playing soccer.

## ACKNOWLEDGEMENTS

First and foremost, I would like to thank my advisor, Dr. Jun Liu for giving me the opportunity to conduct research under him. Whenever I was in a pickle about my research or had a question about my writing, his door was always open. He consistently steered me in the right the direction whenever he thought I needed it.

In addition to my advisor, I would also like to thank the rest of my committee: Dr. Brendan O'Connor and Dr. Xiaoning Jiang.

Research is a team effort, and the constant support of my lab-mates and colleagues made it possible to complete three different projects in the course of two years. Special thanks to Jixiong He and Kyunghoon Kim for being patient with me as I learnt new simulation and modelling techniques. I will be forever be grateful for their insight and advice regarding not only research but several aspects of my time as a graduate student.

Thanks to Kristen Booth, Dr. Srdjan Lukic and FREEDM Systems Center for giving me the opportunity to work on such an interesting application oriented project, which acted as the final piece of the puzzle for my thesis.

Nobody has been more important to me throughout the years of my study, than the members of my family. I would like to thank my parents, for their sacrifices and their support which made it possible for me to travel halfway around the world to pursue my dreams.

## TABLE OF CONTENTS

LIST OF TABLES.....	vi
LIST OF FIGURES.....	vii
<b>Chapter 1: Introduction</b> .....	1
ABSTRACT .....	1
1.1 Need for thermal management .....	1
1.2 Thermal Transport phenomena .....	3
1.3 Objective and Organization of Thesis .....	5
<b>Chapter 2: Optimization of Medium Frequency Transformer with Practical consideration</b> .....	7
ABSTRACT .....	7
2.1 Introduction.....	8
2.2 Optimization Procedure.....	9
2.2.1 Leakage Inductance .....	9
2.2.2 Winding Losses .....	11
2.2.3 Core Losses .....	12
2.2.4 Space Mapping .....	12
2.3 Thermal Model .....	14
2.4 Results and Discussion .....	16
2.5 Conclusion .....	17
<b>Chapter 3: Diffuse mismatch model for calculating interfacial thermal conductance of low dimensional materials using exact dispersion relations</b> .....	28
ABSTRACT .....	28
3.1 Introduction .....	29
3.2 Materials, Methods & Computational Details .....	31
3.3 Results and Discussion .....	33
3.4 Summary .....	36
<b>Chapter 4: Role of Angular Bending Potential in Regulating Thermal Transport in polymers</b> .....	43
ABSTRACT .....	43
4.1 Introduction .....	44
4.2 Materials, Methods & Computational Details .....	46
4.3 Results and Discussion .....	48
4.3.1 Thermal Conductivity.....	48
4.3.2 Structural Analysis.....	50
4.3.3 Phonon Transport Analysis .....	51
4.4 Summary .....	54
<b>Chapter 5: Conclusion and Future Work</b> .....	62
REFERENCES .....	64

## LIST OF TABLES

Table 2.1	Transformer Design Specifications .....	13
Table 2.2	Optimized Transformer Designs .....	14
Table 2.3	Transformer Estimated Temperatures in Degrees Celsius .....	15
Table 3.1	Computational parameters for DFPT calculations .....	37
Table 4.1	Force-field parameters for the bond and angle interactions in our simulation scaled to different values .....	55

## LIST OF FIGURES

Figure 2.1	Three-Level LLC resonant converter .....	22
Figure 2.2	Optimization algorithm for MFT .....	23
Figure 2.3	Physical parameters for leakage inductance calculation .....	24
Figure 2.4	Two-dimensional physical layout for thermal model .....	25
Figure 2.5	Thermal resistive network for MFT design.....	26
Figure 2.6	FEA model of MFT .....	27
Figure 3.1	Phonon Dispersion of Silicon obtained from DFPT calculations .....	38
Figure 3.2	Phonon Dispersion of Graphite obtained from DFPT calculations.....	39
Figure 3.3	Interfacial thermal conductance of the Si-Al interface .....	40
Figure 3.4	Interfacial thermal conductance for (a) Au-graphite and (b) Al-graphite interfaces.....	41
Figure 3.5	Interfacial thermal conductance for the Mos <sub>2</sub> -Al interface .....	42
Figure 4.1	Thermal conductivity in the chain direction as a function of Bond-stretching and angular-bending potential .....	56
Figure 4.2	Thermal conductivity dependence of polyethylene on simulation length in the axial direction .....	57
Figure 4.3	Depiction of morphological changes due to modification of bond and angle potential.....	58
Figure 4.4	Elastic constant along the chain direction as a function of bond and angle potential.....	59
Figure 4.5	Change in frequency of the longitudinal acoustic branch with respect to (a) increasing bond potential and (b) increasing angle potential.....	60
Figure 4.6	Averaged phonon group velocities of the longitudinal acoustic branch corresponding to the phonon dispersion curve of PE, plotted as a function of the bond and angle potentials .....	61

# CHAPTER 1

## INTRODUCTION

In this chapter, we shall discuss the motivation for the thesis and the methods employed in our work. We first take a look at the issue of thermal management in several applications. We shall then introduce the methods employed in the thesis. Finally, a brief outlook of the thesis is provided to give the reader a quick glance into the research challenges that are being tackled.

### 1.1) Need for thermal management

Recent advances in the synthesis and development of materials that are capable of exhibiting a unique set of properties at the nanoscale has led to the miniaturization of electronic devices[1-8]. These nanomaterials have garnered significant interest due to their unique set of properties. For example, organic materials such as carbon nanotubes (CNTs) and graphene have recorded high thermal conductivities of 3500 W/m K and 5800 W/m K, which are much higher than Silicon and Copper which are most used in electronics[3, 7-9]. These impressive thermal properties are complemented by their exceptional strength which makes them attractive candidates for several applications such as flexible electronics, integrated circuit boards and battery electrodes. With the advent of organic electronics, the conventional silicon-based photovoltaic cells are being replaced by flexible and smaller cells. These devices, which are one-tenth the thickness of its larger counterpart, can be used as ultra-thin cells on cloth materials to harness energy. Other applications of organic electronics include organic LEDs and thin film transistors[5, 6, 10-12]. It is well known that polymers at the bulk level have poor thermal properties. But recent studies have exhibited that stretching of polymer nanofibers can yield a thermal conductivity of 100 W/m K which is significantly higher than their bulk counterpart[1, 13, 14]. This opens up

possibilities for potential applications in flexible robotics, phononics, sensors and energy storage. Another class of materials that have emerged as an interesting material choice for nanoelectronics are transition metal dichalcogenides (TMD)[4, 15]. These new materials have high strength, good thermal stability, and are direct band gap semiconductors. While some limitations do exist for synthesis of these materials, they are still regarded as a future material choice owing to their unique set of properties. Even though these nanomaterials mentioned above possess an impressive resume, their application is limited by thermal challenges at the nanoscale which can reverberate to the system-level and cause performance issues.

Modern day electronic devices look to achieve faster and higher computational power at low cost. Higher computational capabilities coupled with shrinking of these devices, leads to heat generation within a smaller volume. The miniaturization is already evident in computers, smartphones, MP3 players and several other electronic devices. This elicits effective cooling to maintain the reliability and efficiency. To understand this problem better, let us consider transistors on an integrated circuit (IC) chip. Moore's Law asserts that the number of transistors on a microchip doubles every two years[16]. This requires engineers to design smaller transistors with higher capabilities. This inadvertently leads to an increase in temperature which is manifested as a "hot-spot". The reliability and efficiency of the system is dictated by these hot-spots. If the temperature cannot be reduced by cooling, then the performance of the device will need to be lowered which is highly disadvantageous[2, 5, 10, 11, 17, 18]. To overcome this challenge, we need to improve the heat spreading capabilities of our system and/or design the system using materials which have excellent thermal properties.

As the device shrinks, the material properties change significantly. For example, the thermal conductivity of a Silicon nanowire is one-tenth of its bulk-counterpart at room

temperature[19]. It is apparent that lower thermal conductivity will make thermal challenges even more daunting. Apart from thermal conductivity, another issue is the thermal interface conductance[20]. The metal-oxide field-effect transistor (MOSFET) is commonly used for switching or amplifying signals in the electronics realm. The design of these transistors consists of several materials deposited on one other, thereby forming “interfaces”. Several of these materials have poor thermal properties, which can lead to an interface resistance which limits the heat spreading capability. For example, the design of flexible electronics involves polymers which possess extremely low thermal conductivity[12]. This can cause thermal management issues and damage the system when operated at high power[10, 11, 17]. It is therefore important to understand how thermal transport occurs at the nanoscale and seek methods to improve the thermal properties of nanomaterials. In order to do so, we must start at the macro-level and analyze how heat transfer changes at the size of the device shrinks. In the next section we shall look at different heat transfer mechanisms and how they are affected with the size of the system.

## 1.2) Thermal transport phenomena

Heat is defined as the energy transfer due to a difference in temperature. There are three modes of heat transfer: conduction, convection and radiation[21-23]. Simply put, conduction is the transfer of energy by material particles as they collide with each other. Conduction is governed by Fourier’s Law, which states that the heat flux is proportional to the negative of the temperature gradient:

$$q = -k \frac{dT}{dx}$$

Here,  $q$  is the heat flux,  $T$  is the temperature,  $x$  is the coordinate in the flow direction, and  $k$  is the thermal conduction of the material through which the heat is flowing.

When we combine conduction and bulk motion of a fluid, we get convection. Heat transfer due to convection occurs when fluid molecules carry the heat away from a surface. The convection heat transfer is given by:

$$Q = h \cdot A \cdot (T_w - T_a)$$

Here,  $A$  is the surface area,  $h$  is the heat transfer coefficient, and,  $T_w$  and  $T_a$  are the temperatures of the surface and fluid respectively.

Unlike conduction and convection, radiation does not require a material medium and transfers the energy by electromagnetic waves. The propagation of these waves can be defined by Maxwell's equations. It depends on the properties of the two surfaces which exchange heat and their geometric arrangement. The radiative heat transfer from a surface X to Y is given by:

$$Q_{XY} = A \cdot \varepsilon \cdot F_{XY} \cdot \sigma \cdot (T_X^4 - T_Y^4)$$

Here,  $A$  and  $\varepsilon$  are the surface area and emissivity of X respectively.  $F_{XY}$  is the shape factor, which depends on the geometric arrangement of the two surfaces, and  $\sigma$  is the Stefan-Boltzmann constant.

This macroscopic view of heat transfer can be used to design analytical and FEA models which can predict the temperature at different points in a device. These “system-level” models function well for components in for a length scale of sub-microns and above. But are these classical theories applicable for smaller components? As the device size shrinks, the microscopic effects that we neglected earlier take center stage[11, 18, 24-27].

As we mentioned earlier, heat conduction occurs due to transfer of energy by random motion of material particles. The nature of these material particles depends on the material. In metals, the primary heat carriers are electrons while in semiconductors and insulators, phonons are responsible for heat transfer. The electrons in a metal are free to traverse a distance longer than the interatomic distance, unless they are scattered. The collisions of these heat carriers with each other and the boundaries of the materials is known as scattering. In insulators, the atoms are joined together by covalent bonds, where the electrons are constrained. The energy is then transferred by lattice vibrations known as phonons. The mean free path of an electron in a bulk metal is typically on the order of 10 to 30 nm, where electron lattice scattering is dominant. With miniaturization, the thickness of the material becomes comparable to the mean free path and boundary scattering becomes important. This phenomenon is defined as the “size-effect” owing to the fact that the physical size influences thermal transport properties. Depending on the method used to manufacture these thin materials, the defect and grain boundary scattering can also affect these heat carriers. Thus, several effects that were not of importance at the macro-scale need to be given full consideration at the micro-scale.

### **1.3) Objective and Organization of the thesis**

The objective of this thesis is to investigate how thermal transport phenomena vary at different length scales. It is rarely the case that all components of a system have the same size. In order to efficiently manage the heating, we need to know how the thermal properties change as the size shrinks. We first conduct a macro-scale thermal analysis of a medium-frequency solid state transformer in Chapter 2. Analytical and FEA models are designed to predict the hot-spot of the transformer core and windings. To ensure maximum accuracy of the FEA models, we incorporate

environmental effects. We also introduce a new framework for optimizing the transformer, which uses a method called space-mapping. Through implementation of this new technique, we can reduce computational time and enhance the accuracy of the design point. The model results are then validated through experimental studies.

In Chapter 3, we move to the micro-scale and investigate a Diffuse Mismatch Model (DMM) used for calculating interfacial conductance between two materials using density functional theory (DFT). A major assumption of this method leads to substantial errors in the predicted values when compared with experimental studies. We propose a new framework which relaxes this assumption and improves the accuracy of the method for predicting thermal conductance of anisotropic materials.

In Chapter 4, we examine the different factors responsible for regulating thermal transport in polymers. Angular bending freedom is one such factor which has not been thoroughly studied in past. A systematic study of polyethylene is conducted, where thermal conductivity is calculated for different angular bending potentials using molecular dynamics simulations.

In Chapter 5, we provide a summary of how thermal transport varies at these different scales and the factors that govern them. Future improvements are then proposed for the different aspects of the thesis.

**CHAPTER 2**  
**OPTIMIZATION OF MEDIUM FREQUENCY TRANSFORMER**  
**WITH PRACTICAL CONSIDERATIONS**

Kristen Booth\*, Harish Subramanyan, Xinyu Liang\*, Jun Liu, Srdjan Srdic\* and Srdjan Lukic\*  
Department of Mechanical and Aerospace Engineering and \*FREEDM Systems Center  
North Carolina State University  
Raleigh, NC USA

*Published in the IEEE Applied Power Electronics Conference, March 17-21, 2019, Anaheim*

**Abstract**

A method to design and optimize a Medium Frequency Transformer (MFT) based on commercially available components and semiconductor and converter constraints is presented. The optimization algorithm is used to redesign the transformer for a scaled-down electric vehicle (EV) fast charger using a three-level resonant circuit topology. The main consideration of this paper is the uncertainty caused by modeling assumptions in optimization algorithms. To reduce this uncertainty, space mapping is used to create an optimized design point. Finally, a comparison of the designs found using the original optimization algorithm and the space mapping technique are compared and analyzed. For simplicity, only a single objective optimization routine is employed.

## 2.1) Introduction

One of the most exciting prospects in the power electronics realm is the advent of a high power converter called solid state transformer (SST), which can replace the traditional bulky transformers[28-35]. SSTs employ a medium-high frequency transformer (MFT) to achieve galvanic isolation and achieve high power density and efficiency and reduced installation costs. However, the smaller size of these transformers leads to increased loss densities. These losses are manifested as increase in temperatures. Excessive temperatures can affect the reliability and efficiency of the system and lead to failure of magnetic components. This poses the challenge of optimizing the transformer to achieve the desired power density and efficiency while minimizing the temperature rise.

Due to the limitations of the models used in the optimization algorithm, most optimization processes for MFTs ignore the realities of hardware design[36-39]. Ignoring these realities will only promote optimal designs that are not feasible in experimental setups. Therefore, it is imperative that power electronics design push toward optimization of realistic designs, including MFTs, that better correlate to the final hardware product.

Every analytical model for MFTs has some limitation as compared to the physical system. Core loss models assume that the flux density is uniform throughout the entire core[40]. Thermal models are currently designed in thermal isolation [41]; however, MFTs are in close proximity to other heat generating sources in the final experimental setup. While improvements to each of these models have been made to reach higher accuracy, the same limiting baseline assumptions remain.

In this work, we provide a detailed thermal analysis of the transformer using two models. We first introduce an analytical thermal model which employs a thermal resistance network to calculate the hot-spots. This model is computationally inexpensive and simple to execute. We then

conduct a finite element analysis (FEA) in ANSYS, which incorporates real-life conditions to improve the accuracy of the predicted temperatures. Research into modeling and parametric uncertainty for power electronic converters is limited. Reference [42] quantified these uncertainties but did not attempt to reduce them. This work aims to quantify and reduce modeling uncertainty in the design of an optimized MFT. The optimization routine is a single-objective Genetic Algorithm (GA), designed for maximum efficiency, to provide a simple discussion of the technique. To reduce modeling uncertainty, we use a technique called Aggressive Space Mapping (ASM) will be used to reduce the model error by coupling the analytical and FEA models.

## **2.2) Optimization Procedure**

The MFT is being designed for a small-scale Electric Vehicle (EV) fast charger. The design specifications for the MFT are given in Table I. The optimization algorithm, depicted in Fig. 1, incorporates an exterior GA with fitness derived through transformer characterization via analytical models. Finally, ASM is used to adjust the analytical models to higher fidelity models of Finite Element Analysis (FEA) to create a realistic final design for the hardware.

The initial magnetics design is created using the conventional methods, as discussed in [43], before the other calculations can take place. In order to reduce computational effort, any unfeasible designs are removed after each step within the transformer characterization process.

### **2.2.1) Leakage Inductance**

The leakage inductance,  $L_\sigma$ , is calculated using the methods described in [44]. The physical parameters required can be found in Fig. 3. For Litz wire, the porosity factor can be calculated as:

$$\eta = \frac{N_{sv} d_{eq}}{h_{core}}, \quad (1)$$

where  $d_{eq} = \sqrt{\pi} / 4 d_r$ . Due to the nonuniform structure of Litz winding, the number of windings oriented horizontally,  $N_{sh}$ , or vertically,  $N_{sv}$ , can be calculated based on the proportional assumption that the total winding cross-sectional profile is followed by the individual strands as

$$K_w = \frac{h_w}{d_{eq}}, \quad (2)$$

Thereby the horizontal and vertical number of windings can be calculated in (3) and (4), respectively, where  $N_s$  is the number of strands in the Litz wire.

$$N_{sh} = \sqrt{\frac{N_s}{K_w}}, \quad (3)$$

$$N_{sv} = \sqrt{K_w N_s}, \quad (4)$$

The Rogowski factor adjusts the equivalent length of the magnetic flux and can be calculated as

$$K_R = 1 - \frac{1 - e^{-\pi h_w / (d_{w,pri} + d_d + d_{w,sec})}}{\pi h_w / (d_{w,pri} + d_d + d_{w,sec})}, \quad (5)$$

which creates the improved height,

$$h_{eq} = \frac{h_w}{K_R}, \quad (6)$$

Therefore, the modified Dowell's method to include these modifications is

$$L_\sigma = \mu_0 N_{pri}^2 \frac{l_T}{h_{eq}} \left[ \frac{d_{eq,pri} N_{sh}}{3} F_{w,pri} + \frac{d_{eq,sec} N_{sh}}{3} F_{w,sec} + d_d + d_{wi,pri} \frac{(N_{sh} - 1)(2N_{sh} - 1)}{6N_{sh}} + d_{wi,sec} \frac{(N_{sh} - 1)(2N_{sh} - 1)}{6N_{sh}} \right], \quad (7)$$

where

$$F_{wy} = \frac{1}{2N_{sh}^2 \Delta} \left[ 4(N_{sh}^2 - 1)\varphi_1 - 2(N_{sh}^2 - 1)\varphi_2 \right], \quad (8)$$

$$\varphi_1 = \frac{\sinh(2\Delta) - \sin(2\Delta)}{\cosh(2\Delta) - \cos(2\Delta)}, \quad (9)$$

$$\varphi_2 = \frac{\sinh(\Delta) - \sin(\Delta)}{\cosh(\Delta) - \cos(\Delta)}, \quad (10)$$

$$\delta = \sqrt{\frac{1}{\pi\mu_0 \eta \sigma f_{sw}}}, \quad (11)$$

$N_{pri}$  is the number of primary winding turns,  $\Delta = \frac{d_{eq}}{\delta}$ ,  $l_t$  is the mean turn length,  $d_d$  is the gap between the primary and secondary windings,  $d_{w,y}$  is the equivalent winding width, and  $d_{wi,y}$  is the width of the dielectric between layers.

### 2.2.2) Winding Losses

Dowell's method is the most commonly used method for generically calculating winding losses in MFTs [45]. However, this optimization is based on a specific Litz wire, so the manufacturer's method is used. The winding losses for Litz wire can be determined using

$$R_{DC} = \frac{R_s (1.015)^{N_B} (1.025)^{N_C}}{N_s}, \quad (12)$$

and

$$R_{AC} = \left[ H + K \left( \frac{N_s \times D_I}{D_O} \right)^2 \right] G R_{DC}, \quad (13)$$

where  $R_{DC}$  is DC resistance [ $\Omega/1000ft$ ],  $R_s$  is the maximum DC resistance,  $R_{AC}$  is AC resistance [ $\Omega/1000ft$ ],  $D_I$  is the individual strand diameter [ $in$ ], and  $D_O$  is entire cable diameter [ $in$ ].

$N_B$  is the bunching operations number,  $N_C$  is the cabling operations number,  $N_s$  is the number of

individual strands, and  $G = \left( \frac{D_l \sqrt{f * 1000}}{10.44} \right)^4$ .  $H$  and  $K$  are given by the manufacturer.

### 2.2.3) Core Losses

The improved General Steinmetz Equation (iGSE) is most commonly used to calculate core losses for MFT optimization algorithms [14]. It is defined as

$$P_C = \frac{1}{T} \int_0^T k_i \left| \frac{dB(t)}{dt} \right|^\alpha (\Delta B)^{\beta-\alpha} dt, \quad (14)$$

where

$$k_i = \frac{K}{(2\pi)^{\alpha-1} \int_0^{2\pi} |\cos \theta|^\alpha 2^{\beta-\alpha} d\theta}, \quad (15)$$

$K$ ,  $\alpha$ , and  $\beta$  are given by the manufacturer. The iGSE is the most widely used core loss empirical method for MFTs as it reduces to a simple equation for square wave excitation found in MF converters. As  $K$  is dependent on the core temperature, an iterative process between the core losses and thermal occurs until equilibrium is reached. For simplicity, the manufacturer's core loss calculation is used in this optimization algorithm for the Ferroxcube 3C90 material.

### 2.2.4) Space Mapping

The basic approach of ASM is to calibrate a coarse (analytical) model to a fine (FEA) model to accelerate design optimization. ASM starts with the optimization argument:

$$x^* \triangleq \arg \min_x U(R(x)), \quad (16)$$

where  $R \in \mathbb{R}^{m \times 1}$  is a vector of  $m$  responses of the model,  $x$  is the vector of  $n$  design parameters, and  $U$  is the objective function.  $x^*$  is the unique optimal solution to be determined.

The fundamental component of SM is that the coarse model and fine model  $x_c$  and  $x_f \in \mathbb{R}^{n \times 1}$ , respectively, can be mapped,  $P$ , as

$$x_c = P(x_f), \quad (17)$$

such that

$$R_c(P(x_f)) \approx R_f(x_f), \quad (18)$$

in a region of interest where  $R_c$  and  $R_f \in \mathbb{R}^{m \times 1}$  are the corresponding response vectors.

As  $R_f(x_f^{m_j+1})$  goes to  $R_c(x_c)$ , then  $x_c^{m_j+1} = P(x_f^{m_j+1})$  approaches  $x_c^*$  as the iteration number reaches a final converging iteration,  $M$ ,

$$\|x_c^{m_j+1} - x_c^*\| \leq \eta \text{ as } j \rightarrow M, \quad (19)$$

where  $\eta$  is a small tolerance. The goal of ASM is to set  $\eta = 0$  in (19). This creates a set of  $n$  nonlinear equations to be set to zero,

$$f = f(x_f) = P(x_f) - x_c^* = 0, \quad (20)$$

Let  $x_f$  be the  $j^{\text{th}}$  iteration to the solution of (20) and  $f$  stand for  $f(x_f^{(j)})$ . The next iteration can be found by a quasi-Newton method

$$x_f^{(j+1)} = x_f^{(j)} + h^{(j)}, \quad (21)$$

where  $h$  is the solution to

$$B^{(j)}h^{(j)} = -f^{(j)}, \quad (22)$$

and  $B$  is an approximation to the Jacobian matrix. For the first iteration,  $B^{(1)}$  is the identity matrix.

For every iteration following,  $B$  is updated by the Broyden formula which can be reduced to

$$B^{(j+1)} = B^{(j)} + \frac{f^{(j+1)}h^{(j)T}}{h^{(j)T}h^{(j)}}, \quad (23)$$

The algorithm is complete when

$$\|f^{(j+1)}\| \leq \eta \quad (24)$$

ASM enables speed within the global design space optimization while improving the accuracy of the optimal design using the fine model.

### 2.3) Thermal Model

The core and winding losses lead to an increase in the operating temperature of the transformer which makes it imperative to calculate the hot-spot. A 2D analytical model is employed which is a simplified version found in [41].

The core is divided into four zones: Upper Yoke, Lower Yoke, Center Limb, and Outer Limb, as shown in Fig. 4. The core losses from each of the zones are modeled as heat sources which are directly proportional to the volume of the corresponding zone. The heat is exchanged between the cores and windings by conduction and radiation. The heat is then lost to the surrounding atmosphere by natural convection and radiation from the front, back, top, and sides of the transformer. It is assumed that the bottom surface of the transformer core is perfectly insulated. This most closely represents the MFT being directly mounted to a surface which will be the case in the experimental setup. The primary and secondary windings are represented using two zones inside the core window.

The well-known electrical circuit analogy is used to couple these six zones where different heat transfer mechanisms are characterized by thermal resistances.

The conduction resistance is defined as

$$R_{cond} = \frac{L}{kA}, \quad (25)$$

where  $k$  is the thermal conductivity,  $A$  is the cross-sectional area, and  $L$  is the length of conduction path.

The convection resistance can be calculated using

$$R_{conv} = \frac{1}{h_{conv}A}, \quad (26)$$

where

$$h_{conv} = \frac{Nu \cdot k}{L_c}, \quad (27)$$

$Nu$  is the Nusselt number,  $L_c$  is the characteristic length, and  $k$  is the thermal conductivity of air at the mean film temperature. To model natural convection from the sides of the transformer, we assumed the surface to be a vertical plate. The Nusselt number is given by:

$$Nu = 0.54 \left( \frac{g \beta (T_a - T_b) L^3 Pr}{\nu^2} \right)^{0.25}, \quad (28)$$

Similarly, convection from the top of the transformer is modeled as a horizontal plate. The Nusselt number is given by:

$$Nu = 0.59 \left( \frac{g \beta (T_a - T_b) L^3 Pr}{\nu^2} \right)^{0.25}, \quad (29)$$

The radiation resistance is given by

$$R_{rad} = \frac{1}{h_{rad}A}, \quad (30)$$

where

$$h_{rad} = \sigma \varepsilon \frac{(T_1^4 - T_2^4)}{(T_1 - T_2)}, \quad (31)$$

$\sigma$  is the Stefan-Boltzmann constant, and  $\epsilon$  is the emissivity.

A detailed resistance network is shown in Fig. 5. The admittance matrix,  $Y$ , was derived using the six nodal points which were selected to best reflect the temperature profile across the transformer. The temperatures at the respective nodes can be obtained using:

$$Q = Y \Delta T, \quad (32)$$

where  $Q$  is the heat loss and  $\Delta T$  is the temperature matrix. Nodes 4 and 6 are expected to be the hot-spots for the core and winding respectively due to the nature of their locations in the resistance network and the power loss generated by the individual components of the MFT.

### 2.3) Results & Discussion

Using the optimization algorithm without and with ASM, the two resulting designs are described and compared. It is important to note that the only design objective is maximizing efficiency; however, multi-objective optimization would render a similar comparison with two differing designs. Both designs are given in Table II for this comparison.

The State of the Art (SOA) design uses only the first two stages of the optimization algorithm in Fig. 2 while the ASM design extends the optimization until the modeled design is properly mapped to the fine model. This extension of the optimization process procures a design that is in better agreement with the FEA output which, in turn, should make the experimental outputs more similar to the expected response of the optimal modeled design than in previous work.

ASM occurs through the core loss calculations. The core losses are space mapped while the winding losses are calculated using the analytical model discussed in Section II. ASM is

considered complete when the difference between the core loss in the analytical model and FEA is less than 0.2 W. This process took two iterations of ASM.

The losses, shown in Table II, are the core losses of each design via the coarse and fine models. It can be seen that the ASM technique puts the core loss of the ASM design within the accepted tolerance limit. While this particular optimization routine does not show a large difference in the core loss between the two designs, it can be assumed that this response difference may increase with more optimization objectives or a larger power rating of the system. This difference is vital to larger systems that require extremely high converter efficiency, such as SSTs or EV fast chargers.

While the overall size of the MFT is relatively unchanged, there is a reduction in the number of turns and switching frequency which reduces the overall losses, shown in the last row of Table II. This also lowers the expected temperature of the MFT. A comparison of the expected temperatures is given in Table III. Therefore, the feasible region of MFT designs for power density using the ASM technique will also be affected by the design adjustment as the temperature of the transformer is dependent upon the losses.

The final design used in the FEA of the MFT is depicted in Fig. 6. Since the thermal model and the leakage inductance calculation assume a full layer, the secondary winding layer is assumed to be complete. This is a baseline assumption that inhibits the modeling of the MFTs. This is a source of modeling error that cannot be removed.

## **2.4) Conclusion**

This work aims to discuss the limitations of analytical optimization algorithms and improve upon them using ASM. The simulated results of these two algorithms using a single objective

example are given and compared. It is shown that two of the three design variables are updated through the ASM technique. Therefore, it can be concluded that using ASM, or a similar technique, is relevant and necessary for building the most optimal design possible.

Future work entails building and comparing the two designs in the experimental setup of the small-scale EV fast charger converter for verification. To further the research into this updated optimization algorithm, a multi-objective optimization algorithm will be employed that will include leakage inductance and power density to see the effects of this method on a larger scale. This background is also enlightening for sensitivity analysis of MFT designs for use in a robust optimization algorithm by incorporating manufacturing tolerances into the overall algorithm.

**Table 2.1:** Transformer Design Specifications

<b>Design Variable</b>	<b>Rating</b>
Input Voltage	600 V
Output Voltage	300 V
Rated Power	6.2 kW
Leakage Inductance ( $L_{\sigma}$ )	30-40 $\mu$ H
Switching Frequency ( $f_{sw}$ )	25-150 kHz

**Table 2.2:** Optimized Transformer Designs

<b>Design Parameters</b>	<b>Before Space Mapping</b>	<b>After Space Mapping</b>
Primary Turns	12	10
Core Sets	6	6
$f_{sw}$ (kHz)	150	125
Analytical Core Loss (W)	4.3	-
FEA Core Loss (W)	3.5	4.4
Total Losses (W)	15.1	13.3

**Table 2.3:** Transformer Estimated Temperatures in Degrees Celsius

<b>Node</b>	<b>Before Space Mapping</b>	<b>After Space Mapping</b>
1	76.43	70.5
2	60.3	56.7
3	55.7	52.7
4	71.5	66.6
5	80.1	73.1
6	82.8	75.7

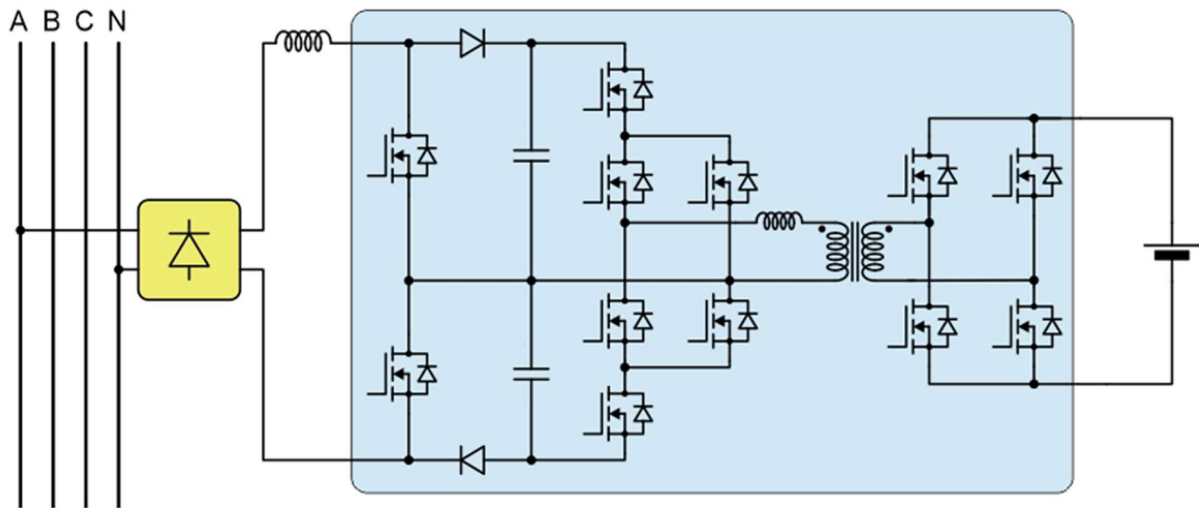


**Figure 2.1** Three-Level LLC resonant converter

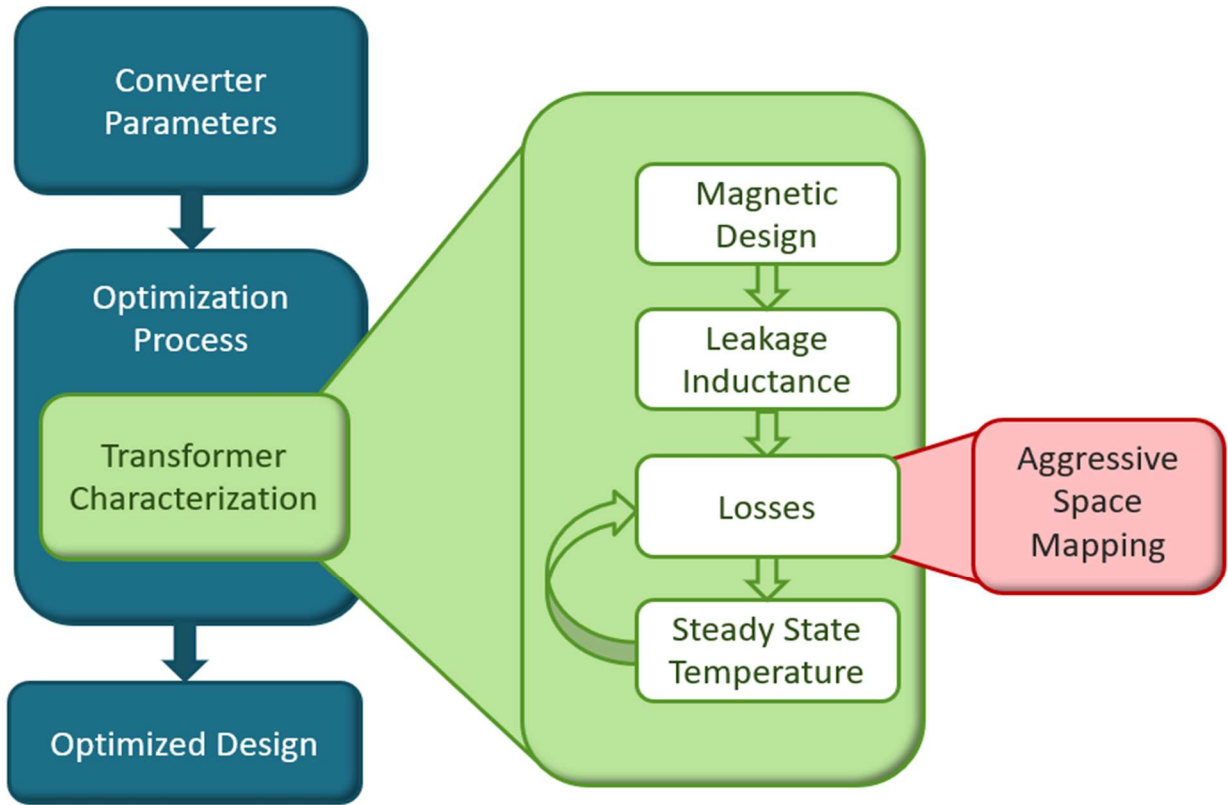


**Figure 2.2** Optimization algorithm for MFT

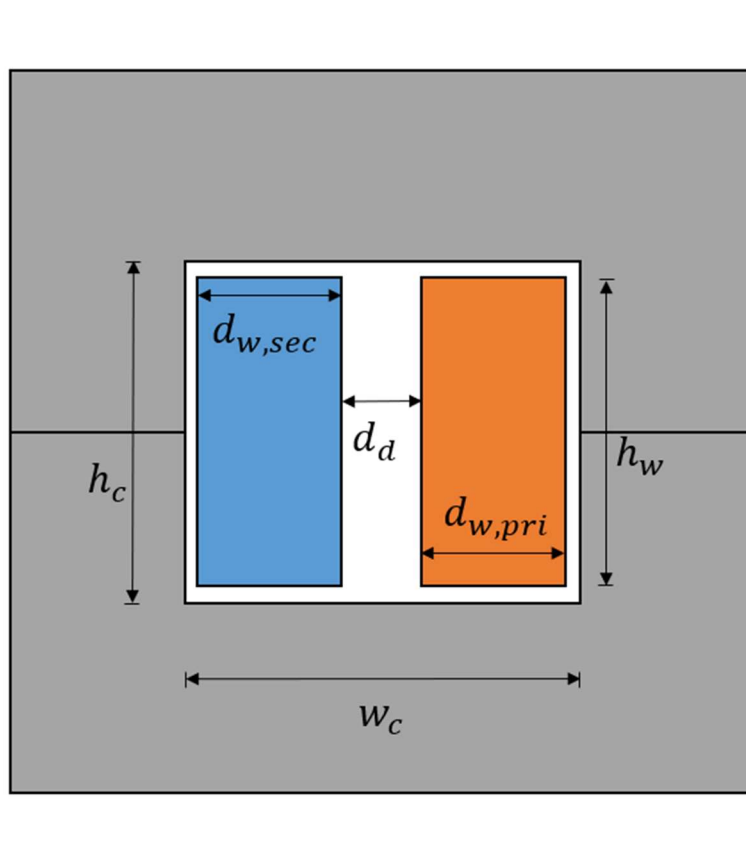


**Figure 2.3** Physical parameters for leakage inductance calculation

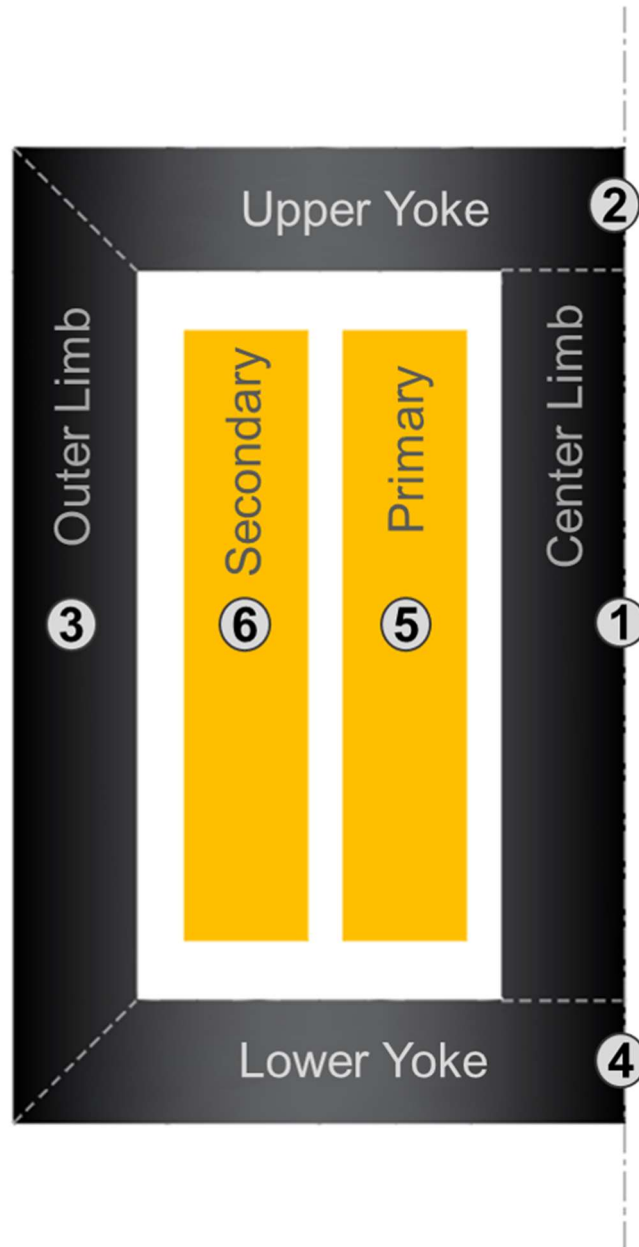


**Figure 2.4** Two dimensional physical layout of thermal model

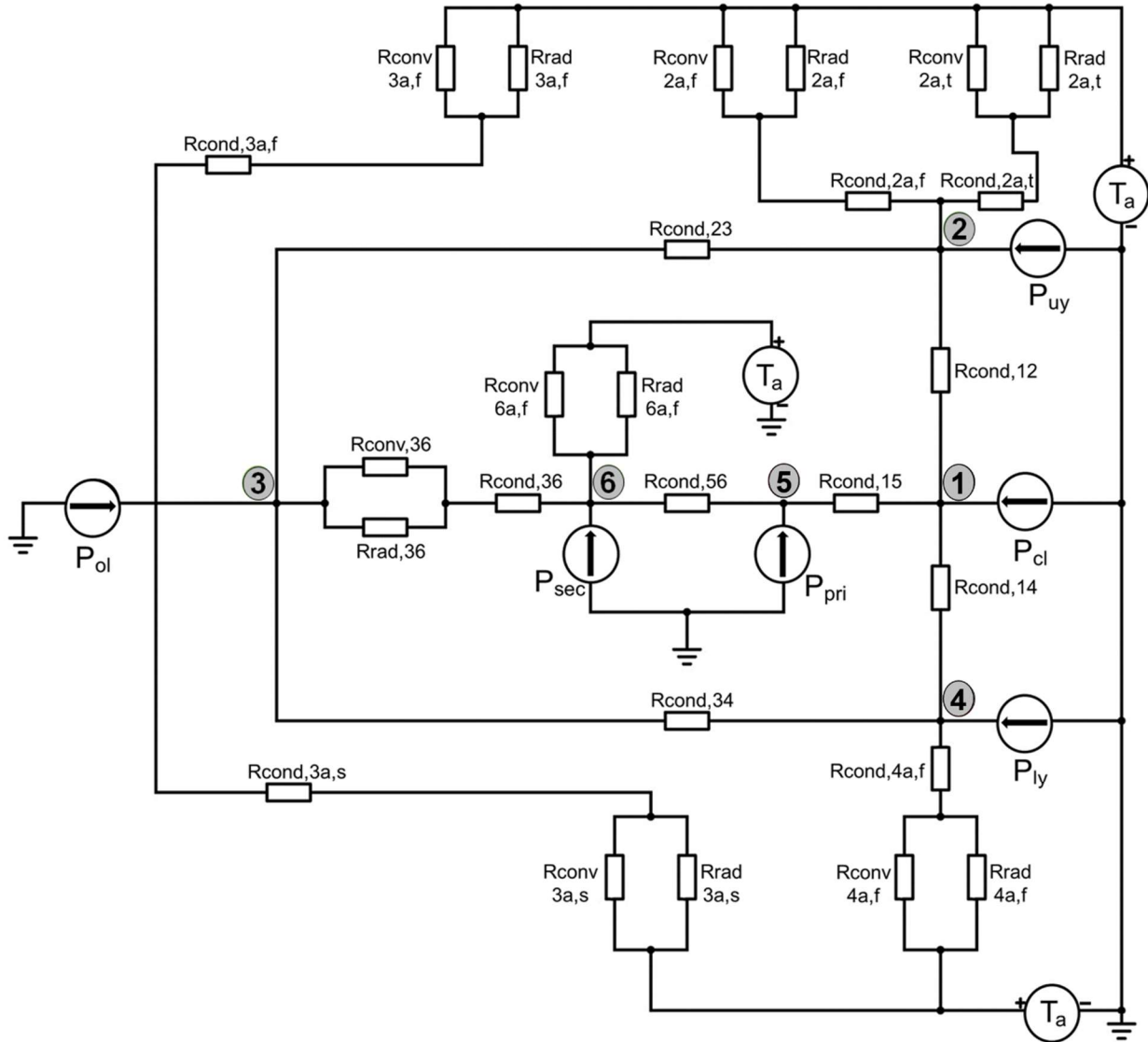


**Figure 2.5** Thermal resistive network for MFT design

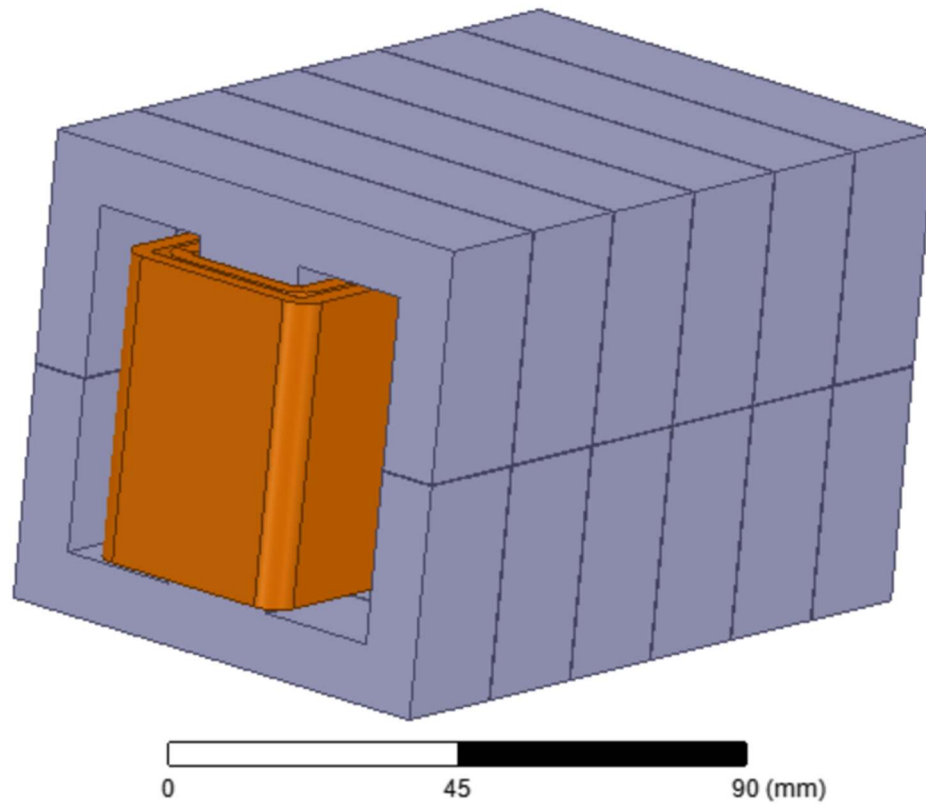


**Figure 2.6** FEA model of MFT

**CHAPTER 3**

**DIFFUSE MISMATCH MODEL FOR CALCULATING INTERFACIAL THERMAL  
CONDUCTANCE OF LOW DIMENSIONAL MATERIALS USING EXACT  
DISPERSION RELATIONS**

**Abstract**

In transistors, two or more different materials form an interface which leads to increased phonon scattering. Several models have been employed in the past to estimate the interfacial thermal conductance between different materials, of which the diffuse mismatch model (DMM) has been generally accepted as reliable. Even though the DMM has been shown to predict the correct order of magnitude in metal interfaces, it is unable to reproduce the same accuracy for 2D anisotropic materials, which have a lot of potential applications . This may be due to the fact that it approximates the phonon dispersion as linear to reduce the computational effort. In this work, we present a modified DMM which utilizes the exact dispersion curves to predict the interfacial thermal conductance. We employ this model to calculate thermal conductance between the interface of 2-D materials such as MoS<sub>2</sub>, Graphite and metals such as Al, Au. We then compare our values with previous literatures that employ linear dispersion and experimental data from time-domain thermoreflectance measurements. We find that using the exact dispersion relations significantly improves the accuracy of the model and that our results agree well with the experimental data. Our findings indicate that it is imperative to use the exact dispersion relation in evaluating the interfacial thermal conductance at most temperatures of interest.

### 3.1) Introduction

The miniaturization of electronic devices continues to achieve faster computational speeds in compact systems[2, 12, 15, 17, 27, 46]. High computational capabilities in a small volume require efficient heat dissipation. The scale down of these devices has led to more interfaces between low dimensional materials and metals present within them. Low dimensional materials such as graphene, graphite and transition metal dichalcogenides (TMDs) have garnered substantial interest since the advent of the mechanical exfoliation method which enables fabrication of layered systems[4, 15, 47-51]. These materials possess a unique set of electronic, optical, mechanical, and thermal properties which find applications in transistors, optoelectronics and thermo-electric devices[2, 5, 10, 12, 17, 52]. The anisotropic nature of these materials renders differing lattice and interfacial thermal transport properties in cross plane and basal plane directions. For example, graphite has an in-plane thermal conductivity of 2000 W/m K in the basal plane but only 7 W/m K in the cross-plane[3]. This opens up the possibility for directional heat transfer and an improved figure of merit in thermo-electric devices. The scattering of energy carriers poses a resistance to heat transfer in solids. The interfaces formed by these materials are spaced at distances smaller than the carrier mean free path (MFP)[26, 27, 46, 52, 53]. As a result, the scattering is dictated by boundaries between the materials rather than the materials themselves. In order to improve heat transfer at these boundaries, a detailed knowledge of the interfacial thermal transport is needed.

A resistance to interfacial thermal transport was first observed as a discontinuity in temperature between the interface of copper and helium[54]. A temperature difference  $\Delta T$  exists between the two solids, which manifests as the thermal boundary resistance  $R$  or thermal boundary conductance  $G$ . The heat flux is given by:

$$Q = \frac{\Delta T}{R} = G \cdot \Delta T, \quad (1)$$

An acoustic mismatch model (AMM) was proposed to explain this phenomenon. It assumes that the phonons incident at an interface undergo specular reflection or transmission and are governed by the principle of continuum mechanics[27, 46, 52, 55]. However, subsequent experiments using phonon pulses and solid liquid interfaces showed that the assumption of specular or non-diffuse phonon reflection and transmission breaks down for high-frequency phonons. The failure of the AMM to accurately predict the thermal conductance at high temperatures led to the diffuse mismatch model (DMM). It assumes that all phonons lose memory of their previous state, undergo elastic scattering and the probability of their transmission across the interface depends on the density of states. An important input of the model is a detailed knowledge of the phonon dispersion relations of the materials involved. For simplicity, the dispersion is usually approximated by a linear relation known as the Debye approximation which has an adverse effect on the accuracy of the DMM. By utilizing the full dispersion to calculate thermal conductance between metal-metal and metal-semiconductor interfaces yielded results that varied significantly from the Debye model[56]. For layered materials such as graphite, an isotropic phonon dispersion predicts thermal conductance with a high factor of error. A general framework was recently proposed which used an anisotropic Debye dispersion to predict thermal conductance in graphite,  $\text{Bi}_2\text{Te}_3$  and high-density polyethylene (HDPE)[57]. This was a significant improvement on the inaccurate isotropic model, which yielded results much closer to experimental values. Following this work, another model was proposed which utilized a truncated linear dispersion to predict lattice and interfacial thermal properties[58]. Though it was able to accurately predict thermal conductivity in the basal plane, the thermal conductance results showed a large discrepancy in comparison to experimental results. This was due to inaccurate approximations of the group velocity. We hope to improve upon these models by incorporating the actual full

dispersion without approximation into the DMM to accurately predict the interfacial thermal conductance[56-65].

The objective of this work is to calculate the thermal conductance of the interface between layered materials and metals using the Diffuse Mismatch Model (DMM). Here we consider the full dispersion of the materials in question without any approximations. We then compare our results with previous anisotropic models and experimental studies.

### 3.2) Materials, Model, and Computational Details

We calculate the interfacial thermal conductance for three interfaces: Al-graphite, Au-graphite, and MoS2-Al. In order to do so, we first need the phonon dispersion curves for the materials forming these interfaces. We used the software Quantum ESPRESSO[66] for this purpose. Density functional perturbation theory (DFPT) calculations are employed to obtain the dynamical matrices in reciprocal space. The dynamical matrix is determined by the change in potential energy by shifting the  $b^{th}$  atom in the  $l^{th}$  unit cell in the  $\alpha^{th}$  direction by a small distance  $\Delta x$ . It is given by:

$$D_q^{3(b-1)+\alpha,3(b'-1)+\beta} = \frac{1}{\sqrt{m_b m_{b'}}} \sum_{l'} \Phi_{b_0;b'l'}^{\alpha\beta} \exp\{i[q \cdot (r_{b'l'} - r_{b_0})]\} \quad (2)$$

By performing a Fourier transformation, we can easily generate the second order interatomic force constants. The phonon modes can be obtained by diagonalization of the dynamical matrix for different q points.

We first performed self-consistent calculations to obtain the converged values for the plan waves cutoff and the k-mesh. The structure was then relaxed to obtain the equilibrium lattice parameters. The computational details for each of these materials are listed in Table 1. After

calculating the second order force constants, we found the dispersion relations at different high-symmetry points and compared them to previous literature for validation[50, 51, 67-74].

We then used Sheng BTE[75] to discretize the Brillouin zone using a dense M-P grid which would ensure accurate comparison of frequencies for two different materials. To calculate thermal conductance, we employed the Diffuse Mismatch Model (DMM)[56-62, 70, 76-79]. For a given interface between two materials A and B, the model assumes that all phonons undergo elastic scattering and lose all memory of their previous state. Let us consider a phonon with wave-vector  $k$  and mode  $i$  that is incident on the interface. The probability that the phonon will be transmitted from A to B is given by:

$$\alpha_{A \rightarrow B}(\omega) = \frac{\Delta K_B [\sum_{j,k} |V(k,j) \cdot \hat{n}|] \delta_{\omega(k,j),\omega'}}{\Delta K_A [\sum_{i,k} |V(k,i) \cdot \hat{n}|] \delta_{\omega(k,i),\omega'} + \Delta K_B [\sum_{j,k} |V(k,j) \cdot \hat{n}|] \delta_{\omega(k,j),\omega'}} \quad (2)$$

where  $\Delta K_A$  and  $\Delta K_B$  are the volumes of the discretized cells pertaining to the high resolution Brillouin zones of A and B. The group velocity and frequency are given by  $V$  and  $\omega$ . The unit vector normal to the interface is given by  $\hat{n}$ . It is important to note here that the Kronecker delta function  $\delta_{\omega(k,i),\omega'}$ , is unity when the frequencies from the two Brillouin zones are equal and zero otherwise. It is evident that  $\alpha$  is purely a function of the frequency. The transmission probability can now be used to find the interfacial thermal conductance, which is given by:

$$G = \frac{1}{2(2\pi)^3} \sum_i \int_k \frac{1}{k_B T^2} \alpha_{A \rightarrow B}(k,i) \times (\bar{h}\omega(k,i))^2 |V(k,i) \cdot \hat{n}| \frac{\exp\left(\frac{\bar{h}\omega(k,i)}{k_B T}\right)}{\left[\exp\left(\frac{\bar{h}\omega(k,i)}{k_B T}\right) - 1\right]^2} dk, \quad (3)$$

Since the phonon loses all memory of its initial state,  $\alpha_{A \rightarrow B} = 1 - \alpha_{B \rightarrow A}$ . In order to obtain the correct conductance, we test different grids for the two Brillouin zones. The choice of the grid depends primarily on the phonon dispersion curves of the respective materials. If the frequency ranges of both A and B are similar, we can select a grid with similar number of q-points. However, if the material A has, say a high frequency range compared to B, the number of q-points for A needs to be greater than that for B. Different grids are tested till we obtain  $G_{AB} = G_{BA}$ . To obtain a quick back-of-the-envelope solution, we can select two grids with same number of q-points and take the average of  $G_{AB}$  and  $G_{BA}$ . This would give us a thermal conductance values which lies in the vicinity of the actual result.

### 3.3) Results and Discussion

To obtain accurate thermal conductance it is important that our dispersion relations are accurate. Figure 1 shows the phonon dispersion curves for Silicon. We compared our results with literature data and experimental results. It is evident that our DFPT calculations agree well with previous results. The tiny discrepancies observed in the longitudinal acoustic (LA) and transverse acoustic (TA) in some of the high symmetry directions can be attributed to our choice of pseudo-potential[80].

Figure 2 shows the dispersion curves for a 2-D material: Graphite. We did a similar comparison with literature data[69]. Our main focus here is on the c-axis which is represent by the gamma-A direction. It is observed that our results are closer to the experimental data. Again, the small discrepancies are due to the choice of pseudo-potential. Nevertheless, we concluded that these results are sufficiently accurate for predicting the thermal conductance.

The frequency and group velocities of each mode is fed into our DMM code which calculates the thermal conductance. Instead of representing these dispersion curves using a polynomial fitting relation, we use a mode-to-mode comparison to calculate which phonons will be transmitted from material A to material B. To validate our DMM code, we compare our results with another similar model that incorporated the full dispersion into their calculations[56]. We study the interface conductance for an Aluminum-Silicon interface. The previous model predicted a thermal conductance of 270 MW/m<sup>2</sup> K at room temperature. Whereas our model calculated the thermal conductance as 304 MW/m<sup>2</sup> K. The values converged for a q-grid of 50 x 50 x 50 applied to the Brillouin zone of both materials involved. The measured value of the thermal conductance of the Al-Si interface using transient thermo-reflectance measurements is around 366 MW/m<sup>2</sup> K at 300 K[81]. The departure of our values from the experimental results can be attributed to the assumption of elastic scattering in the DMM. Furthermore, the values obtained from the experimental measurements depends on the purity of the sample and the surface roughness. Our results can therefore be assumed to be in close vicinity of the true thermal conductance values.

We now proceed to the main objective of this work, calculating thermal conductance for interfaces between layered materials and metals. Using the actual dispersion, we calculated thermal conductance of Aluminum-Graphite and Gold-Graphite interfaces. The converged q-grid for Au-graphite calculations were 50 x 50 x 20 and 30 x 30 x 30 respectively. Whereas for the Al-graphite interface, grids of 40 x 40 x 20 and 40 x 40 x 40 yielded convergence. The results were then compared with Dames' anisotropic model, and experimental results obtained, as shown in Fig 4 (a) and (b). While Chen's and Hongkun's anisotropic DMM predicts the value of thermal conductance as 300 MW/m<sup>2</sup> K and 68.423 MW/m<sup>2</sup> K respectively for Au-graphite interface at room temperature, our model calculates the conductance as 56 MW/m<sup>2</sup> K which is significantly

closer to the experimental value of 30 MW/m<sup>2</sup> K. For the Al-graphite interface, Chen's model predicted the conductance values as 346 MW/m<sup>2</sup> K, Hongkun's model predicts the value as 133.49 MW/m<sup>2</sup> K; the experimental results yielded a value of 49 MW/m<sup>2</sup> K for measurements by Schmidt et.al. and 72.96 MW/m<sup>2</sup> K for measurements by Zhang et.al. Our model calculated thermal conductance as 98 MW/m<sup>2</sup> K, which was again much closer to the experimental results compared to the values predicted by the two anisotropic models[49, 50, 57, 58, 61-64, 68-70, 72, 76, 81-84]. As mentioned before, the experimental results heavily depend on the quality of the sample and it is therefore important to note that our model does extremely well to project thermal conductance values which have the same order of magnitude as the true thermal conductance. Even though our model overpredicts thermal conductance, it can still be regarded as a good framework to study interfacial transport between layered materials and metals. It can also be extended for semiconductor interfaces, as long as we have an accurate phonon dispersion to work with, since the crux of our model is using mode-to-mode comparison.

To illustrate the scope of our model, we calculate thermal conductance for the MoS<sub>2</sub>-Al interface as shown in Fig 5. Our model calculated the value as 29 MW/m<sup>2</sup> K. TDTR measurements predicted values of 56 MW/m<sup>2</sup> K, 25 MW/m<sup>2</sup> K, and 42 MW/m<sup>2</sup> K for different samples. It is again important to note that the quality of the interface plays a key role in the experimental results. Our model is able to effectively predict the correct order of magnitude. It is therefore evident that this framework can be trusted to predict the conductance in close proximity to the true values[47, 48, 51, 77-79].

### **3.4) Summary**

We calculated thermal conductance for Si-Al, Al-graphite, Au-graphite and MoS<sub>2</sub>-Al interfaces. We found that our results agreed well with experimental values. The incorporation of actual dispersion relations without any approximations to the group velocities was critical to the accuracy of the model. The phonon dispersion for most metals are readily available. It will allow us test interfaces between metals and low-dimensional materials. As the only inputs for the model are the phonon dispersion relations of the two materials forming the interface, we can use the model to create a database of thermal conductance values for several material interfaces.

**Table 3.1** Computational parameters for DFPT calculations

<b>Material</b>	<b>Plane-waves energy cutoff (Ry)</b>	<b>k-mesh</b>	<b>Lattice parameters</b>
Silicon	40	20 x 20 x 20	a=10.2023 Å
Aluminum	70	20 x 20 x 20	a=7.4754 Å
Gold	80	10 x 10 x 10	a=7.6798 Å
Molybdenum Sulphide	90	10 x 10 x 4	a=5.9375 Å c/a= 3.8655
Graphite	90	12 x 12 x 4	a=4.6077 Å c/a=2.6549

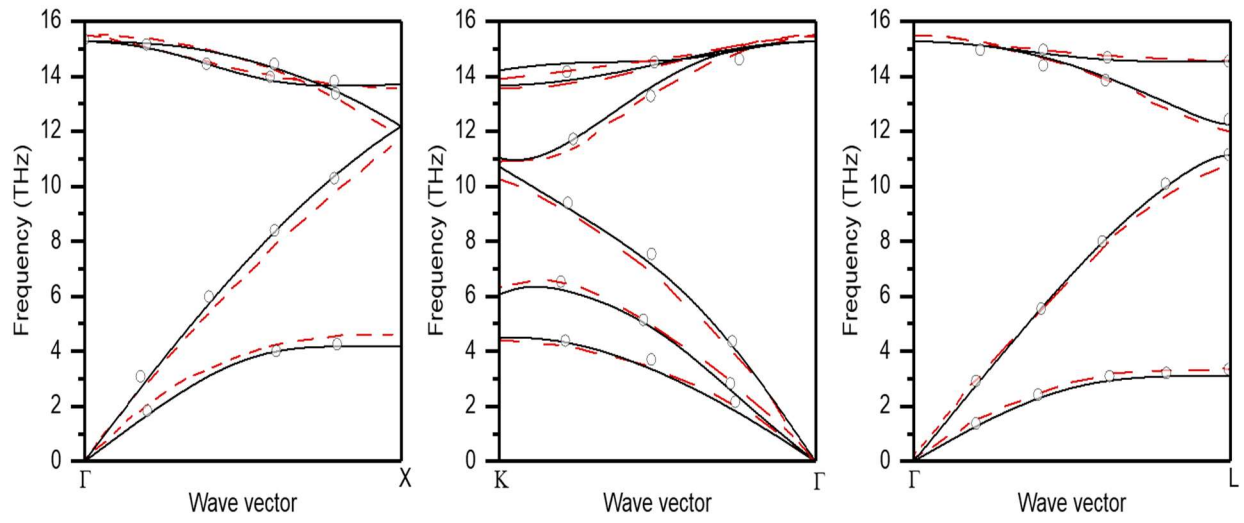


**Figure 3.1** Phonon Dispersion of Silicon obtained from DFPT Calculations (Solid black lines). The dashed dark brown lines represent the literature values from simulation and the hollow black circles are experimental results from inelastic neutron scattering.

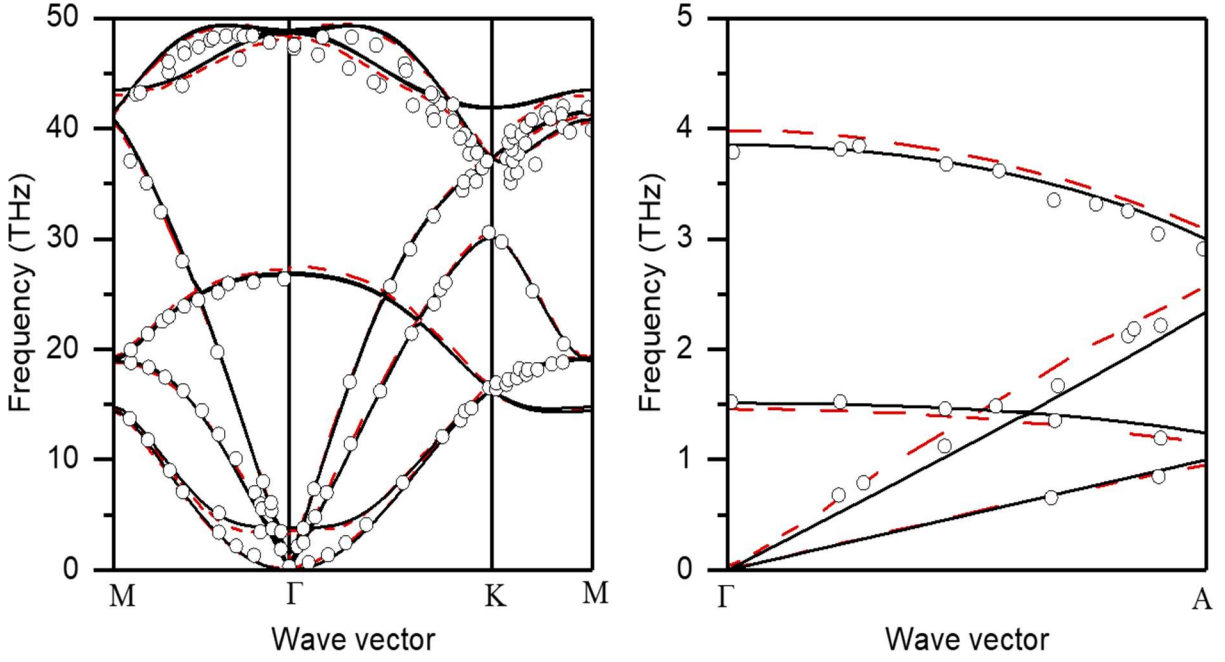


**Figure 3.2** Phonon Dispersion of Graphite obtained from DFPT Calculations (Solid black lines).

The dashed dark brown lines represent the literature values from simulation. The hollow white circles are experimental results from TDTR measurements.

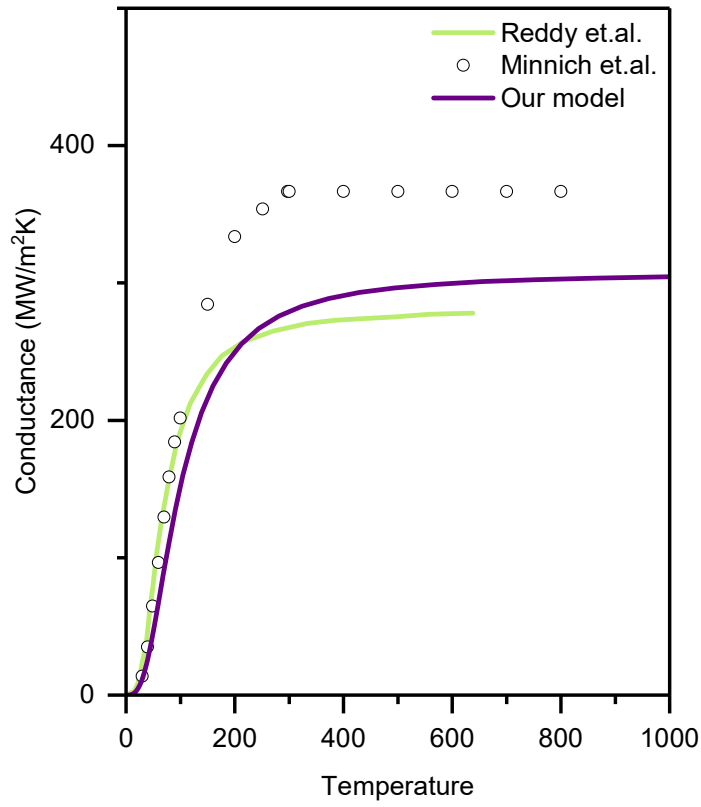


**Figure 3.3** Interfacial thermal conductance of the Si-Al interface. The purple lines represent our model, the light green lines are taken from the Born Von-Karman model used by Reddy et.al. The hollow black circles are the experimental values calculated from TTR measurements by Minnich et.al.

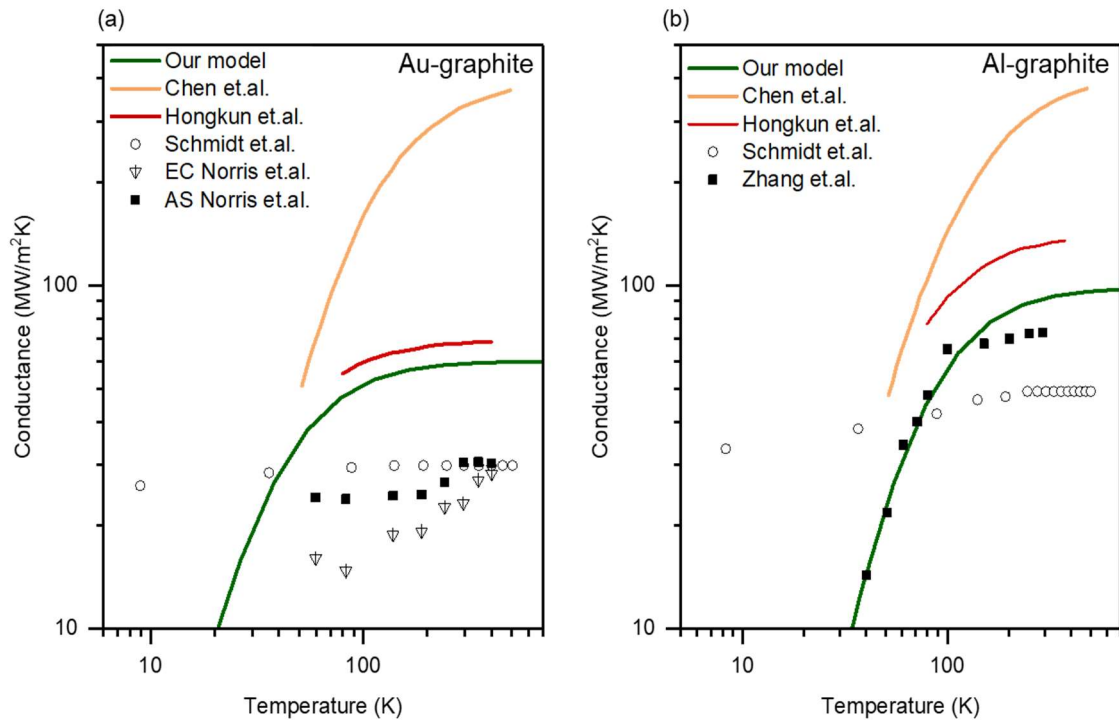


**Figure 3.4** Interfacial thermal conductance for (a) Au-graphite and (b) Al-graphite interfaces.

The dark green lines present our model results which used the actual dispersion. The yellow lines are results taken from Chen’s Anisotropic DMM and the dark brown lines are results taken from Hongkun’s Anisotropic DMM. The black hollow circles are measured values of conductance by Schmidt et.al. using TTR. For the (a) Au-graphite measurements, we also compare the results with electron-cleaved and As-cleaved sample results measured by Norris et.al. using TTR.

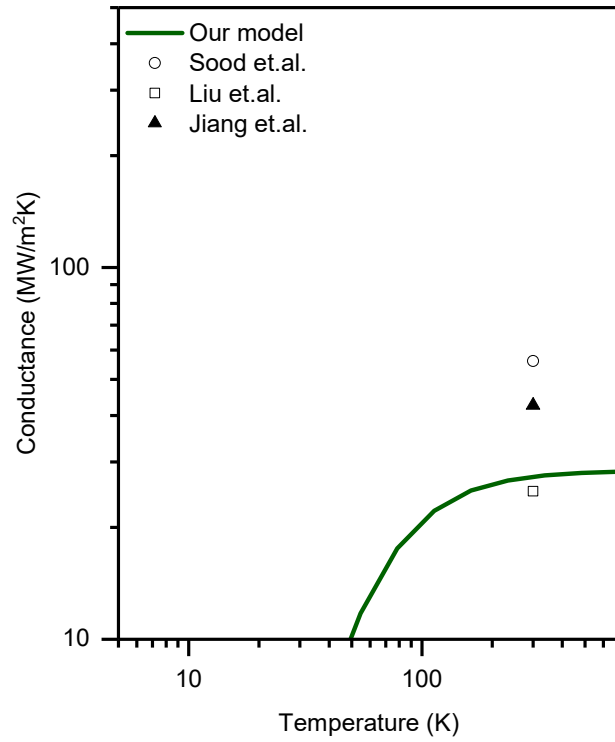


**Figure 3.5** Interfacial thermal conductance for the MoS<sub>2</sub>-Al interface. The dark green lines present our model results which used the actual dispersion. The symbols represent experimental results obtained from TDTR measurements at 300 K.

**CHAPTER 4**  
**ROLE OF ANGULAR BENDING FREEDOM IN REGULATING THERMAL**  
**TRANSPORT IN POLYMERS**

Harish Subramanyan, Weiye Zhang, Jixiong He, Kyunghoon Kim, and Jun Liu  
Department of Mechanical and Aerospace Engineering  
North Carolina State University  
Raleigh, NC USA

*Published in the Journal of Applied Physics, Volume 125, Issue 9*

**Abstract**

Polymers, despite their desirable structural properties, suffer from their low thermal conductivity, which restricts their use. Previous studies have indicated that the strong bond-stretching and angular-bending interactions along the chain are believed to have saturated the maximum achievable thermal conductivity in the along-the-chain direction. Contrary to this belief, our results show an improvement of thermal conductivity. By increasing the bond and angle potential, we studied the effect on the thermal conductivity of polyethylene using non-equilibrium molecular dynamics simulations. In comparison to restricting the bond stretching, we found that restricting angular bending freedom plays a crucial role in improving the thermal transport along the chain. We observed significant changes in the morphology of the polyethylene chains when the angle potential was increased. We also found a remarkable increase in the phonon group velocity accompanied by large shifts in the longitudinal acoustic branch of the dispersion curve. These results when coupled with the structural changes strongly support the argument that thermal conductivity can be controlled by restricting the angular bending freedom.

## 4.1) Introduction

Polymers have immense potential in modern technologies, from soft robotics, and flexible and wearable electronics, to three-dimensional printing and artificial skin, given their unique combinations of properties not available in any other known materials. But those potentials are limited by their low thermal conductivity. Recent efforts in modeling, simulation, manufacturing, and characterization of engineered polymers have largely advanced the fundamental understandings and made progress to improve the thermal conductivity. For example, electrostatically[85] or intermolecular hydrogen-bonding engineered amorphous polymers have been shown[86-88] to have one order of magnitude higher thermal conductivity than the pristine polymers. Xu *et al.* [89] demonstrated that precise control of the conformation of planar backbones together with the inter-chain interactions at the molecular level enables a significant increase in thermal conductivity. The theoretical modeling and simulation work in the past studies[13, 87, 90-96] provide a general guidance that a strong backbone and strong intermolecular interactions is highly beneficial for thermal transport.

The statement of ‘strong backbone’ sometimes can be vague. It is not clear whether ‘strong’ backbone refers to the magnitude of the energy or restricted motion of the backbone. Polymers with larger interatomic forces are usually observed to possess stronger intra- and inter- molecular interactions[97]. These interatomic forces, originating from the electron charge density, are commonly expressed via bonded and non-bonded energies. The total energy  $E$  is given by:

$$E = E_{bonded} + E_{non-bonded} = E_{bond} + E_{angle} + E_{dihedral} + E_{non-bonded} , \quad (1)$$

Therefore, the values of bonded energy, including the bond-stretching  $E_{bond}$ , angular-bending  $E_{angle}$ , and torsional (dihedral) energy  $E_{dihedral}$ , have been commonly adopted to indicate a stiff or

strong backbone, and consequently, a larger thermal conductivity. For example, in the studies of comparing thermal conductivity of single polymer chains[98] and polymer nanofibers[93] among chains with different monomers, larger bond-stretching energy constants have been employed to explain the observed larger thermal conductivity. Another example is the claim[87, 99] that dihedral energy does not contribute directly to the thermal conductivity as its order of magnitude is much smaller than the bond stretching energy and angular bending energy. It is assumed here that the magnitude of the bond energy constant, or bonding stiffness, directly affects the thermal conductivity.

We attempt to revisit this assumption by conducting a systematic study to gain a better understanding of the role that bond stretching and angular bending plays in governing thermal conductivity. Since the magnitude of the bonding-stretching energy constant[100] (299.67 kcal/mol·K) is much higher than the angular-bending energy constant (39.51 kcal/mol·K), it is expected to have a higher contribution to thermal transport, but our results prove otherwise. Though efforts have been made to understand the role of bond-stretching and dihedral energies, there have been no studies to uncover the role of the angular bending energy, which gives us another incentive for this study. We also explored whether varying the angular-bending stiffness causes any chain conformation change and the effect on thermal transport. It is important to determine whether restricting the bending freedom in a polymer chain has a positive effect on the thermal conductivity.

In this paper, we used molecular dynamics to simulate the thermal transport in a simple crystalline polymer. We find that enhancing angular bending stiffness not only increases the thermal conductivity along the chain but has a stronger effect compared to the bond-stretching. This finding reveals the substantial role of maintaining a rigid backbone with restricted bending

freedom, a conformation factor that is far more important than the magnitude of the bonding energy for an individual bond.

#### 4.2) Materials, Models, and Computational Details

Polyethylene (PE) was chosen for this study because of its simple structure. A  $3 \times 4 \times 80$  supercell of crystalline PE was constructed following our previous work.[101] The size of our supercell is  $22.2 \text{ \AA} \times 19.7 \text{ \AA} \times 203.12 \text{ \AA}$ . It consists of 24 chains with 160 carbon atoms each. The Condensed-phase Optimized Molecular Potentials for Atomistic Simulation Studies (COMPASS) force field[100] used the potentials (1) and (2) for bond-stretching and angular-bending, respectively:

$$E_b = k_{2b}(r - r_0)^2 + k_{3b}(r - r_0)^3 + k_{4b}(r - r_0)^4, \quad (2)$$

$$E_a = k_{2a}(\theta - \theta_0)^2 + k_{3a}(\theta - \theta_0)^3 + k_{4a}(\theta - \theta_0)^4. \quad (3)$$

Here,  $r_0$  is the equilibrium bond distance ( $\text{\AA}$ ) and  $\theta_0$  is the equilibrium angle (degrees). We modified the potential by multiplying the coefficients  $k_{2b}$  (energy/distance<sup>2</sup>) and  $k_{2a}$  (energy/rad<sup>2</sup>) by different factors. We ignore the higher order terms as their contribution to the potential is only 1.64 %. It was expected that increasing the potential would make the chain stiffer and enhance phonon transport across the chain.

Non-equilibrium molecular dynamics (NEMD) simulation was employed to calculate the thermal conductivity along the polymer chains. This was accomplished by using the Largescale Atomic/Molecular Massively Parallel Simulator (LAMMPS) package. The NVT (constant mass, volume, and temperature) and NVE (constant mass, volume, and energy) ensemble were used to

relax the structure at 300 K for 1 ns. The values for pressure, temperature and energy were computed to ensure they had minimum fluctuations. The direct NEMD method[94, 102] was used to calculate the thermal conductivity along the chain. This is done by applying a temperature gradient and calculating the heat flux across the gradient. The thermal conductivity[27, 103] can then be found by using Fourier's law of heat conduction:

$$q = - \Lambda_z \frac{dT}{dz} , \quad (4)$$

We use Langevin thermostats to control the local temperatures and establish a heat source and heat sink[104]. The parameters of the thermostat are chosen so that it minimizes the temperature jump at the source and sink. Once the system converges to a steady state, we have a linear temperature gradient and constant heat flux. The direction of our heat flux is along the chain, which is denoted by 'z'. Since we are artificially applying our temperature gradient, a nonlinear temperature profile is observed near the heat source and sink. It occurs due to the mismatch of the lattice vibrations across the temperature-controlled part, and the rest of the region. We calculate the thermal conductivity by fitting only the linear temperature region with an error margin of 5%.

For elastic constant calculation, we first relaxed the structure in the NPT (constant mass, pressure, and temperature) ensemble for 2 ns after energy minimization. We then uniaxially deformed[94, 101] the PE structure along the chain at a constant strain rate of  $4 \times 10^6 \text{ s}^{-1}$  and computed the stress and engineering strain in the z-direction. Here, the engineering strain is defined as the change in length of the chain divided by the original length. The elastic constant was then obtained from the slope of the stress-strain graph.

Lattice dynamics[105-110] was used to identify the different branches of the phonon dispersion curve which is studied later in this work. We use LAMMPS to carry out energy

minimization on the PE structure. The interatomic force constants (IFCs) are then calculated by determining the change in potential energy by shifting the  $b^{th}$  atom in the  $l^{th}$  unit cell in the  $\alpha^{th}$  direction by a small distance  $\Delta x$ . The IFCs are then used to compute the dynamical matrix:

$$D_q^{3(b-1)+\alpha,3(b'-1)+\beta} = \frac{1}{\sqrt{m_b m_b}} \sum_{l'} \Phi_{b0;b'l'}^{\alpha\beta} \exp\{i[q \cdot (r_{b'l'} - r_{b0})]\}. \quad (5)$$

We can now solve the following eigenvalue problem to obtain the eigenvectors  $e_{qv}$  and the frequencies  $\omega_{qv}$ ,

$$\omega_{qv}^2 \cdot e_{qv} = D_q \cdot e_{qv}, \quad (6)$$

### 4.3) Results & Discussion

#### 4.3.1) Thermal conductivity

Figure 1 shows the dependence of thermal conductivity on both bond and angle potentials. The potential values were modified by scaling with factors ranging from 0.4 to 13 in varying increments to explore the behavior of thermal conductivity with a higher resolution. The value of the thermal conductivity for the original PE structure is calculated as 53.7 W/m K. This refers to the thermal conductivity value at the 1k state. Here k refers to the  $k_{2b}$  and  $k_{2a}$  energy constants we defined in the previous section which correspond to bond and angle respectively. We found that our thermal conductivity agreed well with the literature data: Zhang et al. found the thermal conductivity of polyethylene to be 49.2 W/m K, while Luo et al. recorded a value of 52.9 W/m K[87, 99]. We also calculated thermal conductivity for different lengths of the chain to observe any finite size-effects. Figure 2 shows thermal conductivity results for different simulation lengths ranging from 5 nm to

30 nm. We find that the simulated thermal conductivity converges at  $\sim 20$  nm. We now modify the potential by scaling the bond and angle potential constants  $k_{2b}$  and  $k_{2a}$  respectively by different values in separate simulations. As we increase the bond potential, the thermal conductivity fluctuates about the initial value up until 8k and the trend can be treated as a plateau. The thermal conductivity increases rapidly for potential values above 8k up to a value of 89.2 W/m K at 13k. This is due to the increase in the stiffness of the carbon backbone which restricts the chain movement.

For angle, thermal conductivity starts increasing after a potential of 3k. The values increase at a higher rate compared to bond and the plateau trend is only observed for a short range. The thermal conductivity value at 13k is observed to be 139.5 W/m K.

Comparing the initial potential values for bond and angle in Table 1, the notion would be to expect bond to have a stronger correlation with the thermal conductivity as it yields a higher bond energy by virtue of Eq. (2). Increasing the angle potential would restrict the bending movement of the atoms, which has a stronger effect on thermal conductivity. This may be because angle potential governs the movement of three atoms while bond potential relates only two atoms. Another reason could be that the smaller value of angle potential leads to a low angular bending energy as shown in Eq. (3). This allows the chain to bend with more freedom initially. Upon increasing the angle potential, the bending can be constrained and can be constrained to reduce phonon scattering channels, while high bond potential essentially saturates the bond strength and there is no further room for improvement of thermal conductivity. Angle potential seems to play a role in confining the movement of the chain and thus facilitate thermal transport.

### 4.3.2) Structural Analysis

To gain a better understanding of the relationship between thermal conductivity and morphology of the PE backbone, we investigate the effect of seven different potential values each for bond and angle on the bending degree of freedom along the chain. Gaussian fitting of the bending angle probability distribution yielded peaks with centers around 113 degrees. As we increase the bond and angle potential, these peaks become sharper. This effect was quantified by a decrease in the Full Width at Half Maximum (FWHM).[93, 101] It is notable in Figure 3 that increasing the angle potential yields a higher and sharper peak in the distribution as FWHM decreases, when compared to bond potential. The peak becomes 11.3 % sharper for bond and 64 % sharper for angle when potential is increased to 13 times of the original value. This direct effect on the angular bending freedom is somewhat expected. We further explored rotational effects, by conducting a similar study using the dihedral angle probability. This was done to record, if any, indirect effects of the bond and angle potential on the rotational degrees of freedom. The rotational stiffness is enhanced by 2.5% and 6.2 % for bond and angle potential respectively. Though this increase is secondary compared to the angular bending, it is important to note that improving the bond and angle potential do have an indirect effect on the torsional freedom. This indicates that the segmental rotation is moderately restricted due to the ordering of the chain. The restricted rotational freedom reduces the phonon scattering and thus enhances thermal conductivity[111].

Since increasing the potential seems to make the polymer chain stiffer, we expect that increasing the bond and angle potential would yield a stronger backbone. We estimate this effect by calculating the elastic constant along the chain direction. The computational details can be found in the previous section. We expect the bond potential to have a significant effect on the elastic constant as we are directly modifying the bond stretching constant. Figure 4 shows that

elastic constant increases by approximately 78% for both bond and angle potential. The effect of angle potential on the elastic constant was more than expected as changing the angular bending constant was presumed to have minimal effect on the stretching capabilities of the chain. If we were to compare this effect with Figure 3, we can see that the bond stretching constant did not have a similar effect on the bending capabilities of the chain. It is evident that increasing angle potential plays a positive role in increasing the stiffness of the chain in addition to restricting the bending freedom. This advocates for the stronger structural dependence of the PE chain on the angle potential.

### 4.3.3) Phonon transport analysis

To explore the effect of the interatomic potential on the phonon characteristics, we predict the phonon dispersion relations using spectral energy density (SED)[101, 106-108, 112-114]. Our aim is to isolate the contributions by the different modes to the thermal conductivity. To reduce the simulation time, we chose a smaller 3 x 4 x 20 supercell of crystalline polyethylene, consisting of 24 chains with 40 carbon atoms each. The velocities of the atoms were computed using MD simulations in the NVE ensemble at 300 K. We now calculate the spectral energy density along the axial direction for frequencies below 20 THz. The peak and valley profiles are fitted using a Lorentzian distribution function, to obtain the peak center frequency ( $\omega_c$ ) and the half-width ( $\gamma$ ):

$$\Phi(k_z, \omega) = \frac{I}{1 + [(\omega - \omega_c) / \gamma]^2}, \quad (7)$$

The phonon dispersion curve is then obtained by linking the peaks in the SED plots. The phonon group velocity can be calculated using  $\frac{d\omega}{dk_z}$ . The lifetime can be computed using  $1/\omega$ .

We use lattice dynamics calculations to validate our selection of the discrete branches in the dispersion curve.

Using the Boltzmann transport equation, we relate the phonon properties and the axial thermal conductivity. Since our system volume and temperature are constant, we can assume the specific heat to be fixed.

$$\Lambda_z = \sum_k \sum_v C v^2 \tau, \quad (8)$$

We use the phonon dispersion relations obtained from lattice dynamics calculations to find the group velocity. We select the longitudinal acoustic mode (LA), torsional acoustic mode (TWA), and two transverse acoustic modes (TA1 and TA2) and examine the changes exhibited when we increase the potential. From previous literature,[114] we know that the acoustic modes dominate the thermal transport in PE. Furthermore, the LA and TA2 mode have the maximum contribution to the thermal conductivity in crystalline PE. By plotting the dispersion curves at different potentials, we observed that the LA and TA2 branches showed a significant shift from their original position and their slope increased for a higher angle potential whereas increasing bond potential did not harvest any major change. To best describe the nature of the shift, we chose the LA branch as a reference. Figure 5(a) shows the effect of bond potential on the LA branch. The curve depicts a slight shift from its initial position with an increase in its slope. Similarly, Fig. 5(b) shows the effect of angle potential on the LA branch. Here, we can observe that the branch has a significant shift from its initial position which is evident from the high frequency of the LA branch at the 13k potential. To quantify this effect, we now find the group velocity.

The group velocity of the longitudinal acoustic branch was calculated as it has the maximum contribution to thermal conductivity. We use polynomial fitting to connect the different modes of each branch that are obtained from our SED calculations. The group velocity is then obtained then by calculating the slope  $\frac{d\omega}{dk_z}$ . The group velocity is calculated at every allowed mode and then averaged over each branch. Figure 6 depicts a comparison of the group velocity of bond and angle potential for the LA branch. Group velocity shows a large increase for angle potential when compared to bond potential, which indicates the former's ability to enhance thermal transport more than the latter. From Eq. (8), we know that thermal conductivity varies as the square of the phonon velocity. This further confirms that the higher group velocity would increase the thermal conductivity by a large amount. For the bond potential, the group velocity hardly changes for the two modes. The velocity of the LA branch increases by 10.6 % in case of bond potential. Whereas for the angle potential the velocity of the LA branch increases by 78.7 %. This must be the reason for the higher thermal conductivity of PE when we increase the angle potential. It also complements the enhancement of elastic constant in Figure 4.

We now propose that the plateau region observed in Fig. 1 is due to the presence of strong Umklapp scattering[13, 113, 115]. Many phonons scatter by the Umklapp process where the reciprocal lattice vector  $G \neq 0$ . When the increase of potential energy constants is relatively small, the  $TA1+TWA \rightarrow LA$  process is prominent in the chain which reduces the lifetime of the LA phonons and thus counters the effect of high group velocity. As the LA branch shifts away from the initial position and crosses the cutoff frequency of 11 THz with much larger potential energy constants, the Umklapp scattering channels are blocked and we expect the lifetime to increase. But the lifetime results we obtained from our SED calculations do not show any change upon increasing the potential. This may be due to the presence of the flat optical modes which give rise

to new scattering channels such as  $LA+TA_2 \rightarrow LO$  and  $LA+TA_2 \rightarrow TO$  when the acoustic branches shift upwards. This would mean the number of total allowed Umklapp-processes remain the same. The other scattering mechanisms are the normal processes such as  $LA+LA \rightarrow LA$  and  $TWA+TWA \rightarrow TWA$ . These may further aid in yielding a low lifetime. Nevertheless, the dependence of thermal conductivity on lifetime is not comparable to that of the group velocity, which clearly increases upon increasing the potential.

#### 4.4) Summary

In summary, we observed an enhancement of thermal conductivity of crystalline polyethylene when we increased the bond and angle energies. The high phonon group velocity and the morphological effect prove that angle potential has a stronger effect on the thermal conductivity and can be used to govern the thermal transport in polymers, contrary to the belief that the strong interactions along the chain meant that there was no potential for improvement. The combined effect of restricting the bending freedom and improving the elastic constant prove that angle potential plays a crucial role in governing the thermal transport in polymers and cannot be neglected. The role of angular bending freedom in thermal transport begs a more detailed analysis which can be brought about through studying the topologies of different polymers. The question then arises as to whether different topologies of polymers are a key player in the thermal transport problem.

**Table 4.1** Force-field parameters for the bond and angle interactions in our simulation scaled to different values

Scaling Factor	Bond Potential ( $k_{2b}$ )	Angle Potential ( $k_{2a}$ )
0.4	119.87	15.80
0.8	239.73	31.60
1	299.67	39.51
2	599.34	79.02
3	899.01	118.53
4	1198.68	158.04
6	1798.02	237.06

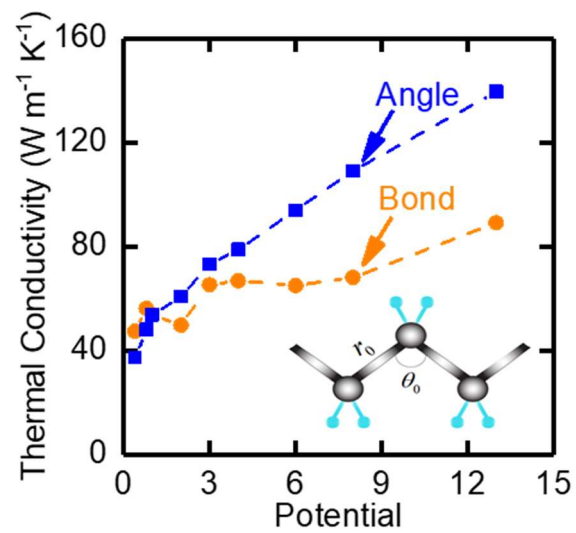


**Figure 4.1** Thermal conductivity in the chain direction as a function of bond-stretching and angular-bending potential. The bond and angle coefficients  $k_2$  are scaled by factors of 0.4, 0.8, 1, 2, 3, 4, 6, 8 and 13 which are represented on the x-axis.

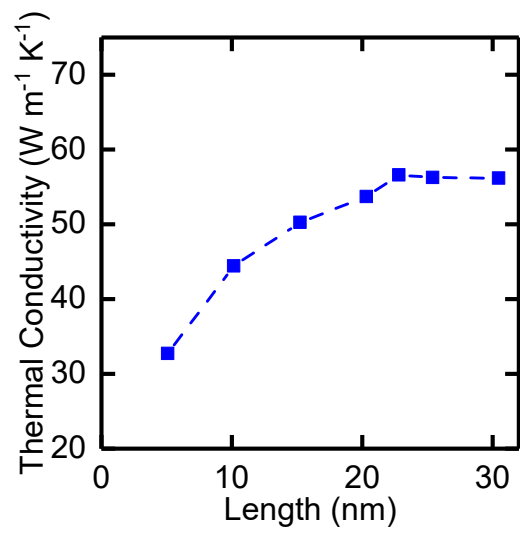


**Figure 4.2** Thermal conductivity dependence of polyethylene on simulation length in the axial direction.

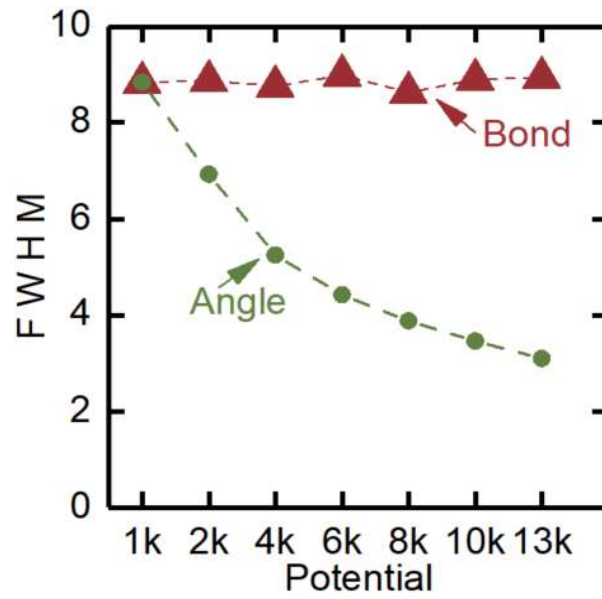


**Figure 4.3** Depiction of morphological changes due to modification of bond and angle potential. The y-axis represents the Full Width at Half Maximum (FWHM) of the bending angle which are calculated at different bond and angle potential values.

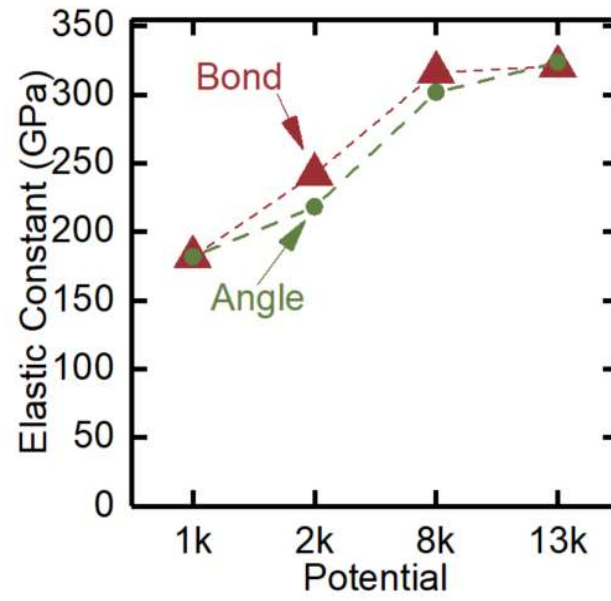


**Figure 4.4** Elastic constant along the chain direction as a function of bond and angle potential.

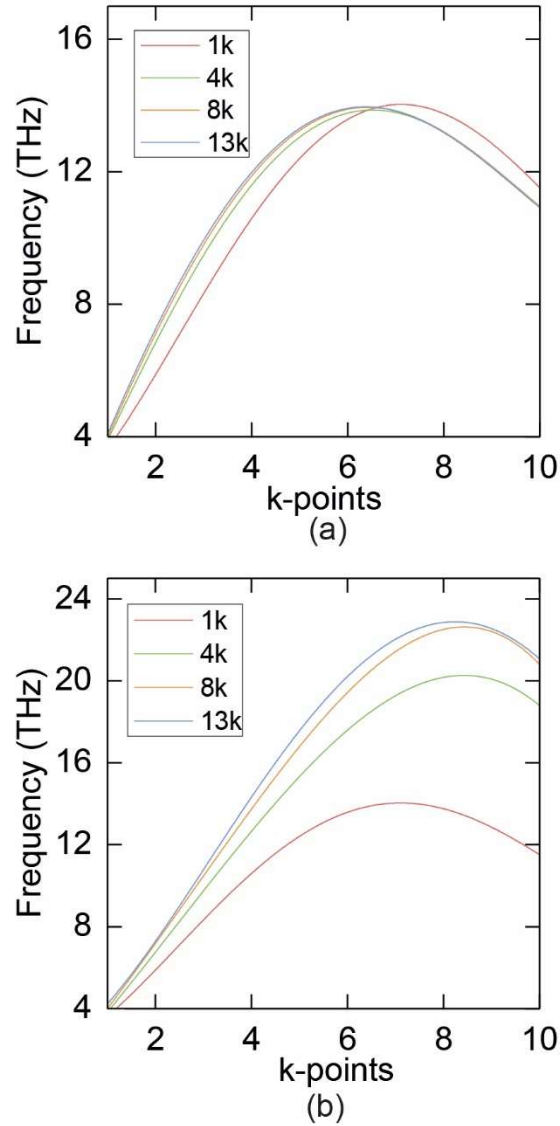


**Figure 4.5** Change in frequency of the longitudinal acoustic branch with respect to (a) increasing bond potential and (b) increasing angle potential. For an increase in bond potential, the frequencies shift upwards near zone center and reach saturation around 8k, while near the zone boundaries the frequencies shift downwards. For an increase in angle potential, the frequencies not only increase near the zone center but display a significant surge near the zone boundaries.

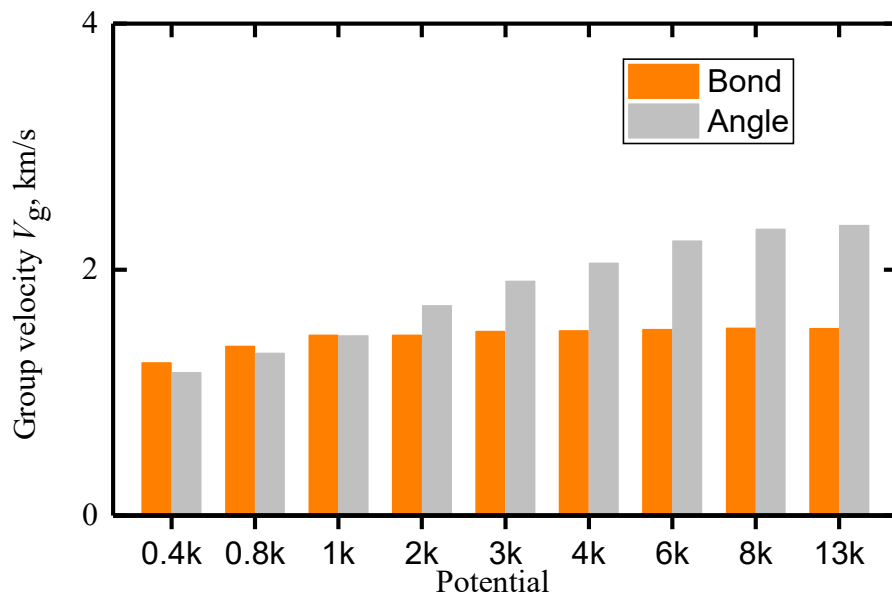


**Figure 4.6** Averaged phonon group velocities of the longitudinal acoustic branch corresponding to the phonon dispersion curve of PE, plotted as a function of the bond and angle potentials.

## CHAPTER 5

### CONCLUSION AND FUTURE WORK

In summary, we investigated thermal transport at different length scales to gain a better understanding of the assumptions and intricacies that underly different heat transfer phenomena. Our first project employed a new method called space mapping to improve the optimization process of a transformer, by combining the speed of the analytical model and the accuracy of the FEA model. The next step would be to introduce environmental effects into the thermal modelling process to represent the real-life conditions. For example, transformers are just one of several electronic components packaged together. These components produce heat which can impact the heat dissipation of the transformer itself. Since the current model assumes thermal isolation, it fails to capture these effects and can lead to an underprediction of the hot-spot temperatures.

As we moved to the micro-scale, we observed that the properties of the heat carriers responsible for conduction regulate the thermal properties of a material. The thermal resistance that exists between the interface of two materials might have been negligible at the macro-scale, but for length scales ranging from nanometers to the sub-micron range, they can play a critical role in improving or impeding heat dissipation. The accuracy of the current model used to predict these interface resistance values was significantly improved by using accurate phonon transport properties. Even though our model significantly improved the accuracy of the predicted values, the margin of error can be further reduced by incorporating inelastic scattering, interfacial bonding and surface roughness into our calculations. The improved accuracy of our model will allow for further fundamental studies to understand the difference in thermal properties for single-layer, double-layer and bulk materials.

Nanoscale thermal transport deviates from the laws of continuum mechanics and is governed by principles of quantum mechanics. When the characteristic dimension of a device becomes comparable to the mean free path of the majority heat carriers, the thermal properties can be significantly different from the bulk counterpart. We utilize this phenomena to improve thermal conductivity of polymers by artificially restricting the angular bending freedom. The realization of an improved structure would need studies of different topologies of polymers. By introducing additional chemical bonds, one might be able to restrict the bending freedom and improve thermal conductivity of polymers experimentally.

By having a thorough knowledge of thermal transport at different length scales, we can make a Macro impact in this new Nano world.

## REFERENCES

1. Kurabayashi, K., *Anisotropic thermal properties of solid polymers*. International Journal of Thermophysics, 2001. **22**(1): p. 277-288.
2. Moore, A.L. and L. Shi, *Emerging challenges and materials for thermal management of electronics*. Materials today, 2014. **17**(4): p. 163-174.
3. Iijima, S., *Helical microtubules of graphitic carbon*. nature, 1991. **354**(6348): p. 56.
4. Sorkin, V., et al., *Nanoscale transition metal dichalcogenides: structures, properties, and applications*. Critical Reviews in Solid State and Materials Sciences, 2014. **39**(5): p. 319-367.
5. Arico, A.S., et al., *Nanostructured materials for advanced energy conversion and storage devices*, in *Materials For Sustainable Energy: A Collection of Peer-Reviewed Research and Review Articles from Nature Publishing Group*. 2011, World Scientific. p. 148-159.
6. Tritt, T., *Recent trends in thermoelectric materials research, part two*. Vol. 70. 2000: Academic Press.
7. Zhang, H., G. Lee, and K. Cho, *Thermal transport in graphene and effects of vacancy defects*. Physical Review B, 2011. **84**(11): p. 115460.
8. Berber, S., Y.-K. Kwon, and D. Tománek, *Unusually high thermal conductivity of carbon nanotubes*. Physical review letters, 2000. **84**(20): p. 4613.
9. Balandin, A.A., et al., *Superior thermal conductivity of single-layer graphene*. Nano letters, 2008. **8**(3): p. 902-907.
10. Pop, E., S. Sinha, and K.E. Goodson, *Heat generation and transport in nanometer-scale transistors*. Proceedings of the IEEE, 2006. **94**(8): p. 1587-1601.

11. Chen, G., *Heat transfer in micro-and nanoscale photonic devices*. Annual Review of Heat Transfer, 1996. **7**(7).
12. Forrest, S.R., *The path to ubiquitous and low-cost organic electronic appliances on plastic*. Nature, 2004. **428**(6986): p. 911.
13. Henry, A. and G. Chen, *Anomalous heat conduction in polyethylene chains: Theory and molecular dynamics simulations*. Physical Review B, 2009. **79**(14): p. 144305.
14. Vadivelu, M., C.R. Kumar, and G.M. Joshi, *Polymer composites for thermal management: a review*. Composite Interfaces, 2016. **23**(9): p. 847-872.
15. Xu, Z., *Heat transport in low-dimensional materials: A review and perspective*. Theoretical and Applied Mechanics Letters, 2016. **6**(3): p. 113-121.
16. Krishnan, S., et al., *Towards a thermal Moore's law*. IEEE Transactions on advanced packaging, 2007. **30**(3): p. 462-474.
17. Schelling, P.K., L. Shi, and K.E. Goodson, *Managing heat for electronics*. Materials Today, 2005. **8**(6): p. 30-35.
18. Shakouri, A., *Nanoscale thermal transport and microrefrigerators on a chip*. Proceedings of the IEEE, 2006. **94**(8): p. 1613-1638.
19. Li, D., et al., *Thermal conductivity of individual silicon nanowires*. Applied Physics Letters, 2003. **83**(14): p. 2934-2936.
20. Prasher, R., *Thermal interface materials: historical perspective, status, and future directions*. Proceedings of the IEEE, 2006. **94**(8): p. 1571-1586.
21. Transport, M.E., C.-L. Tien, A. Majumdar, and FM Gerner. 1998, Taylor & Francis, Washington, DC.
22. Cengel, A., *HEAT TRANSFER*. 2007.

23. Bergman, T.L., et al., *Introduction to heat transfer*. 2011: John Wiley & Sons.
24. Tien, C. and G. Chen, *Challenges in microscale conductive and radiative heat transfer*. *Previews of Heat and Mass Transfer*, 1995. **2**(21): p. 97.
25. Chen, G., *Nanoscale energy transport and conversion: a parallel treatment of electrons, molecules, phonons, and photons*. 2005: Oxford University Press.
26. Luo, T. and G. Chen, *Nanoscale heat transfer—from computation to experiment*. *Physical Chemistry Chemical Physics*, 2013. **15**(10): p. 3389-3412.
27. Cahill, D.G., et al., *Nanoscale thermal transport*. *Journal of applied physics*, 2003. **93**(2): p. 793-818.
28. Huber, J.E., et al., *Analysis and cell-level experimental verification of a 25 kW all-SiC isolated front end 6.6 kV/400 V AC-DC solid-state transformer*. *CPSS Transactions on Power Electronics and Applications*, 2017. **2**(2): p. 140-148.
29. Pefitsis, D., M. Antivachis, and J. Biela. *Auxiliary power supply for medium-voltage modular multilevel converters*. in *2015 17th European Conference on Power Electronics and Applications (EPE'15 ECCE-Europe)*. 2015. IEEE.
30. Bahmani, M.A., T. Thiringer, and M. Kharezy, *Design methodology and optimization of a medium-frequency transformer for high-power dc–dc applications*. *IEEE Transactions on Industry Applications*, 2016. **52**(5): p. 4225-4233.
31. Kouro, S., et al., *Grid-connected photovoltaic systems: An overview of recent research and emerging PV converter technology*. *IEEE Industrial Electronics Magazine*, 2015. **9**(1): p. 47-61.

32. Ortiz, G., et al. *Medium frequency transformers for solid-state-transformer applications— Design and experimental verification*. in *2013 IEEE 10th International Conference on Power Electronics and Drive Systems (PEDS)*. 2013. IEEE.
33. Amaral, F.V., et al., *Operation of a grid-tied cascaded multilevel converter based on a forward solid-state transformer under unbalanced PV power generation*. IEEE Transactions on Industry Applications, 2018. **54**(5): p. 5493-5503.
34. She, X., A.Q. Huang, and R. Burgos, *Review of solid-state transformer technologies and their application in power distribution systems*. IEEE journal of emerging and selected topics in power electronics, 2013. **1**(3): p. 186-198.
35. Srdic, S., et al. *A SiC-based high-performance medium-voltage fast charger for plug-in electric vehicles*. in *2016 IEEE Energy Conversion Congress and Exposition (ECCE)*. 2016. IEEE.
36. Mogorovic, M. and D. Dujic, *100 kW, 10 kHz Medium-Frequency Transformer Design Optimization and Experimental Verification*. IEEE Transactions on Power Electronics, 2019. **34**(2): p. 1696-1708.
37. Villar, I., *Multiphysical characterization of medium-frequency power electronic transformers*. PhD thesis, 2010.
38. Ortiz, G., J. Biela, and J.W. Kolar. *Optimized design of medium frequency transformers with high isolation requirements*. in *IECON 2010-36th Annual Conference on IEEE Industrial Electronics Society*. 2010. IEEE.
39. Kolar, J.W., et al. *Performance trends and limitations of power electronic systems*. in *2010 6th International Conference on Integrated Power Electronics Systems*. 2010. IEEE.

40. Venkatachalam, K., et al. *Accurate prediction of ferrite core loss with nonsinusoidal waveforms using only Steinmetz parameters*. in *2002 IEEE Workshop on Computers in Power Electronics, 2002. Proceedings*. 2002. IEEE.
41. Mogorovic, M. and D. Dujic. *Thermal modeling and experimental verification of an air cooled medium frequency transformer*. in *2017 19th European Conference on Power Electronics and Applications (EPE'17 ECCE Europe)*. 2017. Ieee.
42. Mehrabadi, N.R., et al., *Power electronics modeling and design: Using parametric and model-form uncertainty quantification to assess predictive accuracy of power converter models*. IEEE Power Electronics Magazine, 2017. **4**(4): p. 44-52.
43. Erickson, R.W. and D. Maksimovic, *Fundamentals of power electronics*. 2007: Springer Science & Business Media.
44. Mogorovic, M. and D. Dujic. *Medium frequency transformer leakage inductance modeling and experimental verification*. in *2017 IEEE Energy Conversion Congress and Exposition (ECCE)*. 2017. IEEE.
45. Dowell, P. *Effects of eddy currents in transformer windings*. in *Proceedings of the Institution of Electrical Engineers*. 1966. IET.
46. Smith, A.N. and P.M. Norris, *Microscale heat transfer*. Heat Transfer Handbook, 2003: p. 1309-1357.
47. Dev, D., et al., *High quality gate dielectric/MoS<sub>2</sub> interfaces probed by the conductance method*. Applied Physics Letters, 2018. **112**(23): p. 232101.
48. Liu, J., G.-M. Choi, and D.G. Cahill, *Measurement of the anisotropic thermal conductivity of molybdenum disulfide by the time-resolved magneto-optic Kerr effect*. Journal of Applied Physics, 2014. **116**(23): p. 233107.

49. Norris, P.M., *Modeling Interfacial Thermal Boundary Conductance of Engineered Interfaces*. 2014, VIRGINIA UNIV CHARLOTTESVILLE OFFICE OF SPONSORED PROGRAMS.
50. Minnich, A., *Phonon heat conduction in layered anisotropic crystals*. *Physical Review B*, 2015. **91**(8): p. 085206.
51. Molina-Sanchez, A. and L. Wirtz, *Phonons in single-layer and few-layer MoS<sub>2</sub> and WS<sub>2</sub>*. *Physical Review B*, 2011. **84**(15): p. 155413.
52. Zhou, H. and G. Zhang, *General theories and features of interfacial thermal transport*. *Chinese Physics B*, 2018. **27**(3): p. 034401.
53. Liang, Q., et al., *A detailed study on phonon transport in thin silicon membranes with phononic crystal nanostructures*. *Applied Energy*, 2018. **227**: p. 731-741.
54. Pollack, G.L., *Kapitza resistance*. *Reviews of Modern Physics*, 1969. **41**(1): p. 48.
55. Swartz, E.T. and R.O. Pohl, *Thermal boundary resistance*. *Reviews of modern physics*, 1989. **61**(3): p. 605.
56. Reddy, P., K. Castelino, and A. Majumdar, *Diffuse mismatch model of thermal boundary conductance using exact phonon dispersion*. *Applied Physics Letters*, 2005. **87**(21): p. 211908.
57. Chen, Z., et al., *Anisotropic Debye model for the thermal boundary conductance*. *Physical Review B*, 2013. **87**(12): p. 125426.
58. Li, H., W. Zheng, and Y.K. Koh, *Anisotropic model with truncated linear dispersion for lattice and interfacial thermal transport in layered materials*. *Physical Review Materials*, 2018. **2**(12): p. 123802.

59. Paulatto, L., F. Mauri, and M. Lazzeri, *Anharmonic properties from a generalized third-order ab initio approach: Theory and applications to graphite and graphene*. Physical Review B, 2013. **87**(21): p. 214303.
60. Phelan, P.E., *Application of diffuse mismatch theory to the prediction of thermal boundary resistance in thin-film high-Tc superconductors*. Journal of heat transfer, 1998. **120**(1): p. 37-43.
61. Duda, J.C., et al., *Extension of the diffuse mismatch model for thermal boundary conductance between isotropic and anisotropic materials*. Applied Physics Letters, 2009. **95**(3): p. 031912.
62. Gengler, J.J., et al., *Limited thermal conductance of metal-carbon interfaces*. Journal of Applied Physics, 2012. **112**(9): p. 094904.
63. Yang, F. and C. Dames, *Mean free path spectra as a tool to understand thermal conductivity in bulk and nanostructures*. Physical Review B, 2013. **87**(3): p. 035437.
64. Duda, J.C., et al., *On the assumption of detailed balance in prediction of diffusive transmission probability during interfacial transport*. Nanoscale and Microscale Thermophysical Engineering, 2010. **14**(1): p. 21-33.
65. Kakodkar, R.R. and J.P. Feser, *Probing the validity of the diffuse mismatch model for phonons using atomistic simulations*. Physical Review B, 2017. **95**(12): p. 125434.
66. Giannozzi, P., et al., *QUANTUM ESPRESSO: a modular and open-source software project for quantum simulations of materials*. Journal of physics: Condensed matter, 2009. **21**(39): p. 395502.
67. Park, Y.K. and S.-K. Min, *First-Principles Calculation of the Phonon Dispersion Curves of Silicon*. JOURNAL-KOREAN PHYSICAL SOCIETY, 1997. **31**: p. S267-S270.

68. Duda, J.C., et al., *Inelastic phonon interactions at solid-graphite interfaces*. Superlattices and Microstructures, 2010. **47**(4): p. 550-555.
69. Mohr, M., et al., *Phonon dispersion of graphite by inelastic x-ray scattering*. Physical Review B, 2007. **76**(3): p. 035439.
70. Gu, X., et al., *Phononic thermal properties of two-dimensional materials*. arXiv preprint arXiv:1705.06156, 2017.
71. Duda, J.C., et al., *Role of dispersion on phononic thermal boundary conductance*. Journal of Applied Physics, 2010. **108**(7): p. 073515.
72. Zhang, H., et al., *Temperature-dependent mean free path spectra of thermal phonons along the c-axis of graphite*. Nano letters, 2016. **16**(3): p. 1643-1649.
73. Jain, A. and A.J. McGaughey, *Thermal transport by phonons and electrons in aluminum, silver, and gold from first principles*. Physical Review B, 2016. **93**(8): p. 081206.
74. Lynn, J., H. Smith, and R. Nicklow, *Lattice dynamics of gold*. Physical Review B, 1973. **8**(8): p. 3493.
75. Li, W., et al., *ShengBTE: A solver of the Boltzmann transport equation for phonons*. Computer Physics Communications, 2014. **185**(6): p. 1747-1758.
76. Norris, P.M., et al., *Prediction and measurement of thermal transport across interfaces between isotropic solids and graphitic materials*. Journal of Heat Transfer, 2012. **134**(2): p. 020910.
77. Jiang, P., et al., *Probing Anisotropic Thermal Conductivity of Transition Metal Dichalcogenides MX<sub>2</sub> (M= Mo, W and X= S, Se) using Time-Domain Thermoreflectance*. Advanced Materials, 2017. **29**(36): p. 1701068.

78. Liu, Y., et al., *Thermal conductance of the 2D MoS<sub>2</sub>/h-BN and graphene/h-BN interfaces*. Scientific reports, 2017. **7**: p. 43886.
79. Zhu, L., et al., *Thermal conductivity of biaxial-strained MoS<sub>2</sub>: sensitive strain dependence and size-dependent reduction rate*. Nanotechnology, 2015. **26**(46): p. 465707.
80. Troullier, N. and J.L. Martins, *Efficient pseudopotentials for plane-wave calculations*. Physical review B, 1991. **43**(3): p. 1993.
81. Minnich, A.J., et al., *Thermal conductivity spectroscopy technique to measure phonon mean free paths*. Physical review letters, 2011. **107**(9): p. 095901.
82. Prasher, R., *Thermal boundary resistance and thermal conductivity of multiwalled carbon nanotubes*. Physical Review B, 2008. **77**(7): p. 075424.
83. Schmidt, A.J., et al., *Thermal conductance and phonon transmissivity of metal–graphite interfaces*. Journal of Applied Physics, 2010. **107**(10): p. 104907.
84. Lee, B., et al., *Thermally conductive and electrically insulating EVA composite encapsulants for solar photovoltaic (PV) cell*. eXPRESS Polymer Letters, 2008. **2**(5): p. 357-363.
85. Shanker, A., et al., *High thermal conductivity in electrostatically engineered amorphous polymers*. Science advances, 2017. **3**(7): p. e1700342.
86. Kim, G.-H., et al., *High thermal conductivity in amorphous polymer blends by engineered interchain interactions*. Nature materials, 2015. **14**(3): p. 295.
87. Zhang, T. and T. Luo, *Role of chain morphology and stiffness in thermal conductivity of amorphous polymers*. The Journal of Physical Chemistry B, 2016. **120**(4): p. 803-812.
88. Zhang, T., et al., *Role of hydrogen bonds in thermal transport across hard/soft material interfaces*. ACS applied materials & interfaces, 2016. **8**(48): p. 33326-33334.

89. Xu, Y., et al., *Molecular engineered conjugated polymer with high thermal conductivity*. Science advances, 2018. **4**(3): p. eaar3031.
90. Ma, H. and Z. Tian, *Chain rotation significantly reduces thermal conductivity of single-chain polymers*. Journal of Materials Research, 2018: p. 1-8.
91. Ma, R., et al., *Determining influential descriptors for polymer chain conformation based on empirical force-fields and molecular dynamics simulations*. Chemical Physics Letters, 2018. **704**: p. 49-54.
92. Luo, T., et al., *Molecular dynamics simulation of thermal energy transport in polydimethylsiloxane*. Journal of Applied Physics, 2011. **109**(7): p. 074321.
93. Zhang, T., X. Wu, and T. Luo, *Polymer nanofibers with outstanding thermal conductivity and thermal stability: fundamental linkage between molecular characteristics and macroscopic thermal properties*. The Journal of Physical Chemistry C, 2014. **118**(36): p. 21148-21159.
94. Liu, J. and R. Yang, *Tuning the thermal conductivity of polymers with mechanical strains*. Physical Review B, 2010. **81**(17): p. 174122.
95. Rashidi, V., et al., *Thermal conductance in cross-linked polymers: Effects of non-bonding interactions*. The Journal of Physical Chemistry B, 2017. **121**(17): p. 4600-4609.
96. Robbins, A.B. and A.J. Minnich, *Crystalline polymers with exceptionally low thermal conductivity studied using molecular dynamics*. Applied Physics Letters, 2015. **107**(20): p. 201908.
97. Zhang, T. and T. Luo, *High-contrast, reversible thermal conductivity regulation utilizing the phase transition of polyethylene nanofibers*. ACS nano, 2013. **7**(9): p. 7592-7600.

98. Liu, J. and R. Yang, *Length-dependent thermal conductivity of single extended polymer chains*. Physical Review B, 2012. **86**(10): p. 104307.
99. Zhang, T. and T. Luo, *Morphology-influenced thermal conductivity of polyethylene single chains and crystalline fibers*. Journal of Applied Physics, 2012. **112**(9): p. 094304.
100. Sun, H., *COMPASS: an ab initio force-field optimized for condensed-phase applications overview with details on alkane and benzene compounds*. The Journal of Physical Chemistry B, 1998. **102**(38): p. 7338-7364.
101. He, J., et al., *Strain effects on the anisotropic thermal transport in crystalline polyethylene*. Applied Physics Letters, 2018. **112**(5): p. 051907.
102. Schelling, P.K., S.R. Phillpot, and P. Keblinski, *Comparison of atomic-level simulation methods for computing thermal conductivity*. Physical Review B, 2002. **65**(14): p. 144306.
103. Henry, A., et al., *1D-to-3D transition of phonon heat conduction in polyethylene using molecular dynamics simulations*. Physical Review B, 2010. **82**(14): p. 144308.
104. Chen, J., G. Zhang, and B. Li, *Molecular dynamics simulations of heat conduction in nanostructures: effect of heat bath*. Journal of the Physical Society of Japan, 2010. **79**(7): p. 074604.
105. Shulumba, N., O. Hellman, and A.J. Minnich, *Lattice Thermal Conductivity of Polyethylene Molecular Crystals from First-Principles Including Nuclear Quantum Effects*. Physical review letters, 2017. **119**(18): p. 185901.
106. Ladd, A.J., B. Moran, and W.G. Hoover, *Lattice thermal conductivity: A comparison of molecular dynamics and anharmonic lattice dynamics*. Physical Review B, 1986. **34**(8): p. 5058.

107. McGaughey, A. and J.M. Larkin, *Predicting phonon properties from equilibrium molecular dynamics simulations*. Ann. Rev. Heat Transfer, 2014. **17**: p. 49-87.
108. Feng, T. and X. Ruan, *Prediction of spectral phonon mean free path and thermal conductivity with applications to thermoelectrics and thermal management: a review*. Journal of Nanomaterials, 2014. **2014**.
109. Lindsay, L.R., *Theory of phonon thermal transport in single-walled carbon nanotubes and graphene*. 2010, Boston College. Graduate School of Arts and Sciences.
110. Jain, A., *Thermal Transport in Semiconductors and Metals from first-principles*. 2015.
111. Tu, R., et al., *Impact of torsion and stretching on the thermal conductivity of polyethylene strands*. Applied Physics Letters, 2017. **110**(10): p. 101905.
112. Feng, T., B. Qiu, and X. Ruan, *Anharmonicity and necessity of phonon eigenvectors in the phonon normal mode analysis*. Journal of Applied Physics, 2015. **117**(19): p. 195102.
113. Gu, X. and R. Yang, *First-principles prediction of phononic thermal conductivity of silicene: A comparison with graphene*. Journal of Applied Physics, 2015. **117**(2): p. 025102.
114. Wang, X., M. Kaviany, and B. Huang, *Phonon coupling and transport in individual polyethylene chains: a comparison study with the bulk crystal*. Nanoscale, 2017. **9**(45): p. 18022-18031.
115. Maznev, A. and O. Wright, *Demystifying umklapp vs normal scattering in lattice thermal conductivity*. American journal of physics, 2014. **82**(11): p. 1062-1066.